In compliance with the
Canadian Privacy Legislation
some supporting forms
may have been removed from
this dissertation.

While these forms may be included
in the document page count,
their removal does not represent
any loss of content from the dissertation.

University of Alberta

Photonic Devices in Chalcogenide Glass

by

Robert M. Bryce

A thesis submitted to the Faculty of Graduate Studies and Research in partial fulfillment of the requirements for the degree of Master of Science

Department of Electrical and Computer Engineering

Edmonton, Alberta

Fall 2003

National Library of Canada
Acquisitions and Bibliographic Services
395 Wellington Street
Ottawa ON K1A 0N4
Canada

Bibliothèque nationale du Canada
Acquisisitons et services bibliographiques
395, rue Wellington
Ottawa ON K1A 0N4
Canada

Your file Votre référence
ISBN: 0-612-87727-2
Our file Notre référence
ISBN: 0-612-87727-2

The author has granted a non-exclusive licence allowing the National Library of Canada to reproduce, loan, distribute or sell copies of this thesis in microform, paper or electronic formats.

The author retains ownership of the copyright in this thesis. Neither the thesis nor substantial extracts from it may be printed or otherwise reproduced without the author's permission.

L'auteur a accordé une licence non exclusive permettant à la Bibliothèque nationale du Canada de reproduire, prêter, distribuer ou vendre des copies de cette thèse sous la forme de microfiche/film, de reproduction sur papier ou sur format électronique.

L'auteur conserve la propriété du droit d'auteur qui protège cette thèse. Ni la thèse ni des extraits substantiels de celle-ci ne doivent être imprimés ou aturement reproduits sans son autorisation.

Canada

University of Alberta

Library Release Form

Name of Author: Robert M. Bryce

Title of Thesis: Photonic Devices in Chalcogenide Glass

Degree: Master of Science

Year this Degree Granted: 2003

Permission is hereby granted to the University of Alberta Library to reproduce single copies of this thesis and to lend or sell such copies for private, scholarly or scientific research purposes only.

The author reserves all other publication and other rights in association with the copyright in the thesis, and except as herein before provided, neither the thesis nor any substantial portion thereof may be printed or otherwise reproduced in any material form whatever without the author's prior written permission.

Date: Sept. 19, 2003

University of Alberta

Faculty of Graduate Studies and Research

The undersigned certify that they have read, and recommend to the Faculty of Graduate Studies and Research for acceptance, a thesis entitled Photonic Devices in Chalcogenide Glass submitted by Robert M. Bryce in partial fulfillment of the requirements for the degree of Master of Science.

Date: Sept. 17, 2003

Abstract

Thin films of arsenic triselenide chalcogenide glass were investigated for integrated optics applications. A filter acting as an add-drop multiplexer, for wavelength-routed networks, was designed for construction in arsenic triselenide. Polymers were investigated as an undercladding, and polyamide-imide polymer was demonstrated to be useful, both for use with arsenic triselenide, and for general use in integrated optics. Direct writing of gratings, an important component for integrated optics, was investigated for polymers. Slab and strip waveguiding was demonstrated in arsenic triselenide.

Acknowledgments

I would like to thank my supervisors, for their help, time, and many enlightening discussions. Dr. Jim McMullin allowed me to pursue my interests and make mistakes along the way – thank you for the invaluable experience. Access to your insight into the art and science of photonics has made my time here rewarding. I would like to thank Dr. Ying Tsui for help in the laboratory, advice, and many engaging discussions; I have learned much, both about science, and in general, from you. Finally I would like to thank Dr. Ray DeCorby. The immense amount of time you have spent with me is greatly appreciated. I've gained a more practical and productive perspective from you.

I am indebted to Hue Nguyen: I must thank you for many things. In particular, thank you for your patience in the microfab, help during fabrication, and the vast amount of food of yours that I ate. Working with you was enjoyable and productive.

I would like to thank the students at TRLabs, both for help in research, and for many entertaining occasions. I would especially like to thank P. Nakeeran for all the help in the lab, for his hard work setting up coupling experiments and taking images, as well as for many stimulating discussions.

I would like to thank George Braybrook, of Earth and Atmospheric Sciences, for taking SEM images. I would also like to thank David Clegg, for his advice and expertise in the laboratory.

I owe the greatest debt of gratitude to my beloved, Natasha Parsons, for her support and her love.

Finally, I would like to thank TRLabs for financial support, making this work possible.

Table of Contents

1. Introduction....1
1.1 Thin Optical Films and Integrated Optics....1
1.2 Chalcogenide Glasses for Integrated Optics....2
1.3 Telecommunication Applications of Thin Films....4
1.4 Thesis Outline....6
2. Theory....7
2.1 The Electromagnetic Wave Equation for Homogenous Bulk Media....7
2.2 Slab Waveguiding: The Effective Index and Mode Concepts....9
2.3 The Transfer Matrix Method and the Slab Eigen-equation....13
2.4 The Effective Index Method....17
2.5 Oversized Rib Waveguides....18
2.6 Directional Couplers....20
2.7 Gratings....24
3. Design and Design Considerations....27
3.1 Design Equations....28
3.2 Sensitivity Analysis of Design Equations....30
3.3 Transfer Matrix Simulations....32
3.4 Fan Out Tapering....34
3.5 Mask Design for Devices....36
4. Process Development....40
4.1 Robust Polymer Undercladding....40
4.2 Laser Ablation of Polymers for Grating Fabrication....46
4.3 Slab Waveguiding in Chalcogenide Films....52
4.4 Inverted Rib Structures....55
4.5 Photodoped and Photodarkened Structures....61
5. Summary and Recommendations....66
5.1 Overview of Significant Results....66
5.2 Suggestions for Future Work....67
References....69
Appendix 1: Oversized Rib Waveguide Criteria....74
References....79
Appendix 2: Swanepoel's Method....81
References....83

List of Tables

Table 3.5.1 Representative device parameters. For 1.55 μm wavelength the design equations found result in devices with parameters of this order. 38

Table 4.2.1 Polymer Ablation Thresholds. 48

Table A1.1 Comparison of scaling rule sets. Here air clad 8 μm film with TE polarized 1.55 μm light is assumed. 77

Table A1.2 Minimum Δ required for simplified rules. Here the minimum Δ for the simplified rules to be valid within a given measure is found, for deep rib guides excited with 1.55 μm TE polarized light. 78

List of Figures

Figure 1.2.1 The chalcogen group. Glasses formed with chalcogens (S, Se, Te) are similar to oxides, but their large shell structures have increased polarizability. This, in combination with their structural flexibility, leads to pronounced optical effects. 3

Figure 1.2.2 Grating assisted add-drop filter. Two waveguides in close proximity will transfer energy between them. Placing a grating in the mid region will cause wavelength selective reflection. By making the structure physically symmetric, identical add-drop characteristics result. 5

Figure 2.2.1 Slab waveguide. Cross sectional view of an idealized slab waveguide of thickness d. Each region is homogeneous, so that there is no variation in the y or z directions. In practice a slab waveguide is often grown on a substrate, so that it is often the case that $n_2>n_3>n_1$ 10

Figure 2.2.2 Waveguiding in slab. A slab confines light, allowing waveguiding. In the ray picture (top) reflection at the boundaries traps the light, while solution of Helmholtz equation leads to a modal view (bottom). 10

Figure 2.2.3 Wavevector in slab waveguide. When light is confined to a slab waveguide the total wave vector can be split into longitudinal, β, and transverse, κ, components. 11

Figure 2.3.1 Wave propagation in homogeneous 1-D media. (a) Light can propagate either forward or backwards in bulk 1-D media, (b) at an interface reflection will occur, and energy will be redistributed into different modes. 14

Figure 2.3.2 Slab Geometry. The transfer matrix method can be used to describe one-dimensional wave propagation. For waveguiding we require $E(x_1)^-$ and $E(x_2)^+$ to be zero (light does not leave the structure). 15

Figure 2.4.1 Schematic of the Effective Index Method. The cross section of the 3-D waveguide is split into slab waveguide regions and corresponding effective indices are found. Using these indices allows the 3-D structure to be represented by an equivalent 2-D system; a thin film slab replaces the 3-D structure. 17

Figure 2.5.1: Cross Section of Inverted Rib Waveguide. Scaling the rib width (w), side slab height (h), and rib height (H) according to the oversized rib criteria allows single mode operation for large cross sections. 19

Figure 2.6.1: Effective index model of a directional coupler. Waveguides of width d separated by a distance s can be modeled as a stack of slabs. 21

Figure 3.1 Grating assisted add-drop filter. Two waveguides in close proximity will transfer energy between them. Placing a grating in the mid region will cause wavelength selective reflection. By making the structure physically symmetric, identical add-drop characteristics result. 27

Figure 3.2.1: Sensitivity on waveguide spacing and film thickness. Note that these effects are of approximately equal strength. 31

Figure 3.3.1: Transfer Matrix Method simulation of grating assisted filter. A drop wavelength of 1.55 μm was selected. Note the flat "top hat" response near this wavelength, and the ringing at the edges of the selected band. 33

Figure 3.3.2: Gaussian grating profile. Varying a grating with a Gaussian envelope can be used to suppress "ringing", and thereby reduce cross-talk into adjacent channels. Here an exaggerated profile is shown to illustrate the modulation. The data points correspond to grating high and low regions, and alternates between "zero" (background index) and a Gaussian modulated high index value. 33

Figure 3.3.3: Effect of Gaussian grating profile. Ringing is induced by sudden truncation of gratings (left image), by varying the grating within a Gaussian envelope the ringing can be reduced (right image). 34

Figure 3.4.1: Beam propagation verification of taper methodology. A linear directional coupler with 100% power transfer between waveguides was designed (top), a tapered equivalent structure was found keeping phase shift experienced between supermodes equal. BPM analysis on the tapered section (bottom) was performed, were it can be seen that power transfers between waveguides (the bottom right image is a close up of the end region of the bottom left hand image). The waveguide structure is outlined in gold, and the optical power is in false colour scale (blue – low power, red – high power). 36

Figure 3.5.1: Mask Layout. The mask consists of 25 directional coupler based devices, which are duplicated to make 50 device structures. In (a) the directional couplers can be seen in the center of the layout area. Large boxes are located on the left and right edges and the bottom, in order to facilitate alignment. Linear waveguides are located across the top of the layout, in order to allow testing. In (b) a magnified section showing detail of the directional couplers is shown. Alignment marks, and the patterns for device identification can be seen. 39

Figure 4.1.1. Spin curve of Torlon on test wafers. Note that the spin characteristics are nominally described by power law behaviour. 43

Figure 4.1.2. SEM micrograph of alignment mark eched into Torlon. Inset: magnified detail of etch wall. There is little roughness on the etched surface, though striations from the Au mask can be clearly seen. 44

Figure 4.1.3 Torlon index data. Solvay's application bulletin reports an index value of 1.656 for bulk material at an unspecified wavelength, collaborating with values measured here for thin films. 45

Figure 4.1.4. Loss trace of Torlon Waveguide on BCB undercladding. Inset: End view of an inverted rib waveguide, with Torlon core layer and BCB undercladding. The presence of speckles in the film indicates particulate scattering centers. 46

Figure 4.2.1 Experimental Setup. A laser pulse from the KrF laser passes through a 1cmX1cm aperture (A), focuses through a lens (L), is split into two with a beam splitter (BS), and brought back together with two mirrors (M) onto a target (T) film. 47

Figure 4.2.2 AFM micrograph of ablated grating in Mylar film. Here multiple shots were made and the deterioration of the polymer can be seen. 49

Figure 4.2.3 SEM Micrograph of ablated Mylar grating. Scale bar for the left hand image is 1 μm, and 100 nm for the right hand image. In the right hand image the feather like features are part of the Mylar sheet film, while the spots appear to be molten plastic backsplattered onto the surface. Reducing the period results in reduced grating depth (strength). 49

Figure 4.2.4 SEM Micrograph of ablated BCB Grating. Scale bar 1 μm. Shallow gratings of ~ 800 nm period can be clearly seen. 50

Figure 4.2.5 SEM Micrograph of ablated Torlon grating. Scale bar 100 nm. Debris is loosely bound; cleaning samples with alcohol washes the debris away. 50

Figure 4.2.6. AFM micrographs of Mylar films. Sheet Mylar (left hand image) has ~ 20 nm crystals embedded within the film. Note the lack of crystals in spun cast Mylar (right hand image). 51

Figure 4.2.7. SEM Micrograph of ablated gratings on spun cast Mylar. Scale bar 1 μm. Note the lack of back splatter, versus Mylar sheets. 52

Figure 4.3.1: Top view of diced slab structure on Si wafer at 100X magnification. A sharp interface was obtained. 53

Figure 4.3.2: End facet of slab waveguide system, under 100X magnification. A distinct and smooth facet was obtained after cleaving and the chalcogenide layer was undamaged over most of the cut, with the exception of locations were the Si wafer exhibited mechanical damage. The Torlon layer is ~ 6 μm thick. 54

Figure 4.3.3: Coupling 830 nm light into slab waveguide. The loss streak can be seen propagating along the slab. Notice the absence of speckles in the film, indicating a corresponding absence of imperfection and scattering centers. 55

Figure 4.4.1 Plasma Etch of Torlon. 10 μm wide and 1 μm deep trench test structure for inverted rib waveguides. 56

Figure 4.4.2 Plasma Etch of BCB. 4 μm wide and 0.5 μm deep trench test structure for inverted rib waveguides. 57

Figure 4.4.3 Plasma etch of oxide. Inset shows post treatment by chemical etch to remove pillars. The "bevel" corner is ~ 1.5 μm long. Substantial roughness remains even after chemical treatment. 57

Figure 4.4.4 Chalcogenide glass deposited on Torlon. A 4 μm wide and 0.5 μm deep trench was plasma etched into Torlon. 10 μm of chalcogenide was evaporated on top. Surface roughness in the trench is transferred thought the glass, but within the film no pillar structure exists. 58

Figure 4.4.5 Chalcogenide glass deposited on oxide. A 4 μm wide and 0.5 μm deep trench was chemically etched and chalcogenide was evaporated on top. Note the mismatch between the undercladding and chalcogenide film, visibly demonstrating expansion effects. 59

Figure 4.4.6 Annealing induced fracture of chalcogenide. Oxide underclad samples experienced cracking within waveguide sections due to stress release. The thermal expansion mismatch between oxide and chalcogenide causes stress during heating and cooling, the waveguides are weak regions that act as breakage points. 60

Fig. 4.5.1: Photodarkened Waveguide. A broadband illumination source (tungsten lamp) was used to photodarken chalcogenide glass through a mask. The upper image is a top view of 830 nm light being coupled into the waveguiding structure and the lower image is of the waveguide output. 62

Fig. 4.5.2: Photodarkened Directional Coupler. The upper image is a top view of 1550 nm light being coupled into the waveguiding structure defined with broadband illumination (tungsten lamp); the light is coupled in the upper right corner and propagates to the lower left. The diced edges can be observed in the corners of the upper image. The lower image is of the end view (output) of the directional coupler, note the faint illumination line corresponding to the chalcogenide film and the bright spots corresponding to waveguides (250 μm separation). 62

Fig. 4.5.3 Photodarkened and etched test features. Alignment mark (top) and directional coupler regions (bottom) are defined by photodarkening followed by a chemical etch. Optical microscope images (left) demonstrate the clear features obtained, while optical spectrophotometery (right) shows high etch contrast is obtained. 64

Figure A1.1: Cross Section of Inverted Rib Waveguide. Scaling the rib width (w), side slab height (h), and rib height (H) according to the oversized rib criteria allows single mode operation for large cross sections. 74

Figure A2.1 Transmission response of a thin film. The measured transmission for a ~1.1 μm thick chalcogenide film demonstrates the interference pattern typical of thin films. 81

List of Abbreviations

AFM	Atomic Force Microscope
Al	Aluminum
As	Arsenic
Au	Gold
BCB	Benzocyclobutene
BPM	Beam Prorogation Method
CCD	Coupled Charge Device
CMT	Coupled Mode Theory
DMAC	N,N-dimethylacetamide
DMF	N,N-dimethylforamide
DNA	Deoxyribose Nucleic Acid
Ga	Gallium
Ge	Germanium
Hg	Mercury
In	Indium
IPA	Isopropyl Alcohol
KrF	Krypton Fluoride
La	Lanthanum
MEMS	Micro-Electromechanical Systems
MMI	Multi-Mode Interference
N	Nitrogen
P	Phosphorus
PAI	Polyamide-imide
PET	Polyethylene-telephthalate
PI	Polyimide
PTFE	Polytetrafluoroethylene
RIE	Reactive Ion Etch
S	Sulfur

Se	Selenium
SEM	Scanning Electron Microscope
Si	Silicon
SiO_2	Silicon Dioxide
SOI	Silicon on Insulator
TE	Transverse Electric
Te	Tellurium
TM	Transverse Magnetic
TMM	Transfer Matrix Method
WDM	Wavelength Division Multiplexing

1. Introduction

1.1 Thin Optical Films and Integrated Optics

Patterned thin films can be used to trap light and define "optical circuits". Integrated optics is the study of devices built from such structures, where the film thickness is comparable to the optical wavelengths involved [1], [2].

Optical films have stringent requirements:

- optical losses should be small;
- films must be mechanically stable; with good adhesion to other films and substrates, resistances to cracking/scratches, low stress, etc.;
- films must be resistant to ambient as well as processing conditions, including elevated temperatures and strong chemicals;
- uniform thickness and refractive indices are required;
- films must be amenable to patterning of structures; and
- films must work with at least one other material of differing refractive index, in order to confine light.

These requirements are strongly affected by a films microstructure. Optical films are thin (~ μm scaled) and accurate control of the microstructure is often unattainable, making it difficult to fabricate films that meet the requirements for optical use. This situation has hindered progress in integrated optics, and optical film research has stimulated the development of thin film science and technology. For this reason the investigation of materials for thin film optics continues to form an important research area.

Several materials that partially meet the requirements exist, and have lead to useful integrated optic devices [2]; often these materials are compatible with few other materials. This significantly reduces the functionality achievable on a single integrated device. Furthermore, suitable materials are often prohibitively expensive.

1.2 Chalcogenide Glasses for Integrated Optics

Chalcogenide glasses exhibit properties between that of crystalline semiconductors and polymers. Chalcogenides are semiconductors, with an optical bandgap (E_g ~2 eV). On the other hand, chalcogenides have a locally flexible, soft, structure, similar to polymers. Due to their flexibility, exposure to near bandgap light can cause bond modification, inducing structural changes.

Chalcogenides are formed from group IV elements in the periodic table (the chalcogen group, Fig. 1.2.1), and consist of materials with S, Se, and Te components[1]. Chalcogenide glasses are similar to oxides, but exhibit pronounced optical properties. The flexible structure of chalcogenides is due to lone pair electrons and a low coordination number[2]. Experimental investigations indicate that photoirradiation with near bandgap light increases the structural disorder, by broadening the bond angle distribution [3], [4]. This can in turn lead to expansion, as well as modification of the refractive index. During exposure the bond rearrangement can allow chemical bonding with introduced species (often metals) and material flow. The local structural changes (modification of the refractive index, expansion) are reversible by annealing near the glass transition temperature [5].

---

[1] Oxides are excluded by convention, largely due to early, and extensive, development of this field. Po is a radioisotope, and is therefore excluded in practice.

[2] Lone pair electrons are nonbonding electrons. Their effect is to modify the orbital of bonding electrons. As a low coordination number exists in chalcogenides (2 covalent bonds, leading to average coordination numbers of ~2-3 in chalcogenide glasses) the result is a flexible structure of directional bonds. Water (with its oxygen "chalcogen") is a prototypical example of the rich structures that can arise from these effects, with chains, sheets, cages, and crystal structures possible.

8 O
16 S
34 Se
52 Te
84 Po

Figure 1.2.1 The chalcogen group. Glasses formed with chalcogens (S, Se, Te) are similar to oxides, but their large shell structures have increased polarizability. This, in combination with their structural flexibility, leads to pronounced optical effects.

In addition to these photoinduced changes, chalcogenides have high refractive index, are transparent in the infrared, and display large nonlinearities (~500X that of silica glass [6]). These properties indicate chalcogenide glasses may be suitable for integrated optics – with the ability to optically write (and thermally erase) structures, create dense placement of devices, allow low-loss operation, and form all optical logic networks.

Arsenic triselenide (As_2Se_3) glass films are studied in the present work. This material is simple to deposit, with thermally evaporated films adhering to many substrates. These films also exhibit large photodarkening (~2% change in refractive index can be induced) and do not photoexpand [7]. This glass is therefore promising as an optical film, and forms the focus of a research thrust at TRLabs. Fabrication of holographically written waveguides using 633 nm light has been demonstrated [8], suggesting these gratings can be integrated into devices.

Arsenic triselenide has some drawbacks: the material is toxic, and it is difficult to incorporate rare earths into As_2Se_3 films (rare earths are useful for creating optical sources and amplifiers). In general, chalcogenides are also fragile, being easily damaged mechanically and chemically. For example, during this work it was found that water strongly attacked the glass, causing it to peel away from substrates. Acetone, a common chemical used in processing, has also been found to attack As_2Se_3. Alcohols, in particular

isopropyl alcohol (IPA), were not observed to react with As_2Se_3, and an IPA rinse followed by air-gun drying can be used to clean samples.

Chalcogenides have a large coefficient of thermal expansion, typically an order of magnitude larger than technologically important substrates [9]. For As_2Se_3 the thermal expansion coefficient is 21 ppm/°C, while the glass transition temperature is 200 °C [10]. This can result in large thermal stresses occurring during heat-dependent processing steps.

Chalcogenide glasses have many desirable optical properties, but are fragile. In addition chalcogenides are often toxic[3], leading to health concerns. In the present work, a study of the suitability of As_2Se_3 glass films for integrated optic devices is undertaken.

1.3 Telecommunication Applications of Thin Films

Telecommunications currently drives much of integrated optics research, due to the large number of users per device offsetting costs. The adaptation of the wavelength division multiplexing (WDM) scheme, where communication channels are encoded on different wavelengths, has lead to a bandwidth increase that has enabled optical components to penetrate the telecommunications network. The optical device niche opened up by WDM has resulted in an enormous range of device options to filter and manipulate optical signals [2].

Key elements in WDM networks are multiplexers/demultiplexers, which combine and separate different wavelengths. These elements are required to place information on, and remove information from, a network.

---

[3] Arsenic, often used in chalcogenide materials, is particularly concerning. Arsenic readily forms complexes with oxygen and sulfur (i.e. is incorporated into tissue), and is linked to DNA damage.

Optical add-drop filters, for use as WDM multiplexers/demultiplexers, can be fabricated by placing two waveguides in close proximity, and adding a grating region (Fig. 1.2.1). The close proximity of the waveguides causes energy to flow between the waveguides, in a periodic manner, as the light travels along the structure. Adding a grating will cause reflection at the Bragg wavelength, imposing wavelength selectivity[4].

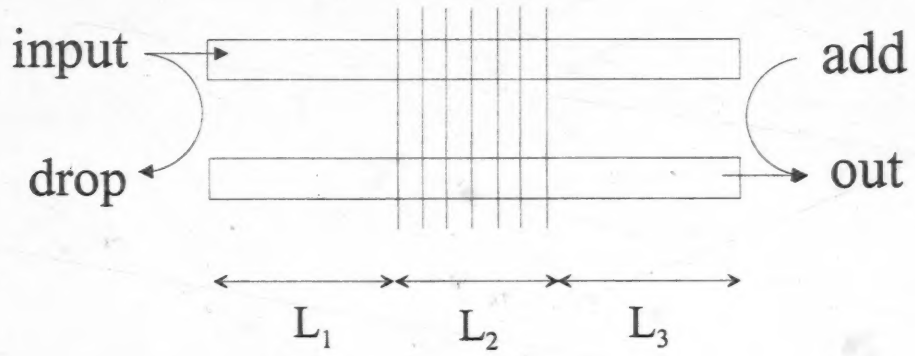

Figure 1.2.2 Grating assisted add-drop filter. Two waveguides in close proximity will transfer energy between them. Placing a grating in the mid region will cause wavelength selective reflection. By making the structure physically symmetric, identical add-drop characteristics result.

Away from the Bragg wavelength the effect of the grating is weak, and the total length of the device ($L_1+L_2+L_3$) can be set to force all the light to exit the device, located in one waveguide. At the Bragg wavelength the grating will act as a distributed mirror, and tuning the length of the nongrating regions allows all the light reflected to exit the device on the other waveguide, in the opposite direction. By balancing these requirements with the requirement that that grating region be long enough to prevent the Bragg wavelength from leaking through results in grating-assisted optical add-drop filters for use in WDM networks. These types of devices have been widely realized in optical fibres (see for

[4] The Bragg condition is $2n\Lambda=m\lambda$, where n is the refractive index, Λ the spatial period, m an integer, and λ the optical wavelength. The wavelength selective nature of a grating (periodic variation in refractive index) is clearly observable in periodic media, such as feathers, butterfly wings, shells, and compact disks. Modifying the interaction angle of the light on the structure (changing the periodicity seen by the light) will result in observation of different reflected colours. This iridescent effect is as useful as it is striking, and is used, for example, by butterflies to control their wing temperature. For a set angle, as is the case for light trapped in a waveguide, a given wavelength (the Bragg wavelength) will be reflected, enforcing a wavelength selective process.

example [11]). Fibre devices are bulky, motivating research into integrated versions of this device.

In the present work, the suitability of arsenic triselenide glass for integrated optics is undertaken, centering on the construction of a grating-assisted optical add-drop filter.

1.4 Thesis Outline

The electromagnetic theory describing optical thin films is introduced in Chapter 2. The wave equation for thin slabs is given, and a method to approximate three-dimensional structures with slabs is outlined. The effect of periodic variations in a material is briefly discussed.

Chapter 3 makes use of this theory for the design and simulation of a grating-assisted add-drop filter. Design equations are developed, and some modifications to allow implementation are performed. Using these developments a mask was designed, which was fabricated by Adtech Photomask.

In Chapter 4 process development is discussed. As chalcogenide glasses have large thermal expansion, polymers are investigated as undercladdings. The direct formation of gratings, by ablation of polymers, is then discussed. The creation of slab waveguides consisting of arsenic triselenide films on polymer and oxide undercladding was demonstrated, indicating that these films can be used for optical applications. Fabrication of inverted rib structures was attempted using thermal evaporation. Failure to achieve adequate structures lead to attempts to spin-cast arsenic triselenide. Suitable inverted structures could not be formed, and photodarkened structures were investigated instead.

The final chapter summarizes the achievements made, and makes recommendations for future work. The successful fabrication of a device was not realized, and combination of the processes for a complete prototype remains as a challenge for future work.

2. Theory

The electromagnetic wave equation allows the interaction between light and structured material to be described. Thin films that confine light are the basic building block of integrated optical devices. Propagation in slabs can be solved in terms of simple functions, but in general the wave equation must be numerically solved.

2.1 The Electromagnetic Wave Equation for Homogenous Bulk Media

From Maxwell's electromagnetic equations [12], the wave equation describing the electric field $\overline{E}$ can be derived. In a region of space where the dielectric permittivity ε and the magnetic permeability μ are constants the wave equation is found to be

$$\nabla^2 \overline{E} - \varepsilon\mu \frac{\partial^2 \overline{E}}{\partial t^2} = 0, \qquad (2.1.1)$$

where ∇^2 is the Laplacian (spatial derivative operator).

Comparing to general wave equations it is recognized that the wave has a velocity given by

$$v = \frac{1}{\sqrt{\varepsilon\mu}}. \qquad (2.1.2)$$

In vacuum, this velocity is the speed of light ($c \sim 3*10^8$ m/s). In dielectrics $\mu=\mu_0$ and $\varepsilon=\varepsilon_r\varepsilon_0$ where μ_0 and ε_0 are the permeability and permittivity in vacuum, respectively. The velocity of a wave scales by

$$v = \frac{1}{\sqrt{\varepsilon_r}\sqrt{\varepsilon_0 \mu_0}} = \frac{c}{n}, \qquad (2.1.3)$$

where the refractive index n is introduced. The refractive index succinctly describes the interaction of electromagnetic waves and matter, for weak interactions.

A simple, yet elegant, model for understanding and describing the refractive index is the spring model [13]. Here the molecules making up a medium are considered to be electrons bound to nuclei by springs. Oscillating electromagnetic fields cause the electrons to vibrate, where the driving field couples to the matter in a frequency dependent manner[1]. A complex interchange of energy between the driving field, the electrons, and fields re-emitted by electrons exists, and, in general, the refractive index is a complicated function. Many theoretical models exist to describe the refractive index, but in practice the refractive index must be measured and fit to models. By using a complex function, the imaginary component can account for loss experienced by a wave during propagation.

Considering monochromatic waves of angular frequency $\omega = 2\pi f = \frac{2\pi}{\lambda} v$, where λ is the wavelength and f the frequency, we introduce plane waves of the form

$$E \sim e^{i(\bar{k} \bullet \bar{z} - \omega t)}, \qquad (2.1.4)$$

where $\bar{k}$ is the wavevector. Substitution of plane wave fields (2.1.4) into the wave equation (2.1.1) leads to the Helmholtz equation

[1] This model allows one to quantify the "weak" interaction required for the refractive index to be a function of frequency only. If electrons are perturbed, with energies near the ionization energy of the molecule, the refractive becomes dependent on intensity, and the material is considered to be in a "nonlinear" regime. If the intensity is further increased electrons can be stripped from their molecules, causing material damage and modification. Similarly bond rearrangement can occur under suitable conditions. Furthermore thermal changes can modify the refractive index (for example, absorbed light can heat the material); modification in density due to acoustic vibrations can occur; and so on. In general the refractive index depends on all the parameters of the system, but it is often the case that the parameters are fixed, or have small effect, and the electric fields used are "weak". This situation allows these parameters to be ignored.

$$\nabla^2 E + k^2 E = 0 . \qquad (2.1.5)$$

The wave number $k = |\vec{k}|$ is described by the dispersion equation

$$k = \frac{\omega}{c} n = \frac{2\pi}{\lambda_0} n , \qquad (2.1.6)$$

where λ_0 is the wavelength in vacuum. In practice, the waves are referred to by their vacuum wavelength. By convention, vacuum variables are denoted with the subscript 0.

Helmholtz's equation (2.1.5) underpins much of the modeling done in integrated optics, understanding of the assumptions made for its derivation is therefore important. First: matter is assumed to be spatially homogeneous, secondly: pure frequency plane waves are assumed. Strictly speaking, Helmholtz's equation only applies to monochromatic waves in bulk media, but it is found, in practice, that as long as these criteria are not strongly violated a good description is provided [14].

The refractive index plays the central role in describing the interaction between matter and electromagnetic waves. In the next section, we will see how this concept can be generalized, allowing a description of structure to be incorporated into the refractive index.

2.2 Slab Waveguiding: The Effective Index and Mode Concepts

The Helmholtz equation (2.1.5) can be cast into a form explicitly containing the refractive index

$$\nabla^2 \vec{E} + k_0^2 n^2 \vec{E} = \nabla^2 \vec{E} + \left(\frac{2\pi}{\lambda_0} n\right)^2 \vec{E} = 0 . \qquad (2.2.1)$$

The refractive index acts like a (inverse) potential acting on the electromagnetic wave. Trapping of waves can occur by creating a high indexed region embedded in a low indexed background. The simplest such structure is an infinite slab waveguide (Fig. 2.2.1), which has no variation in the y or z directions.

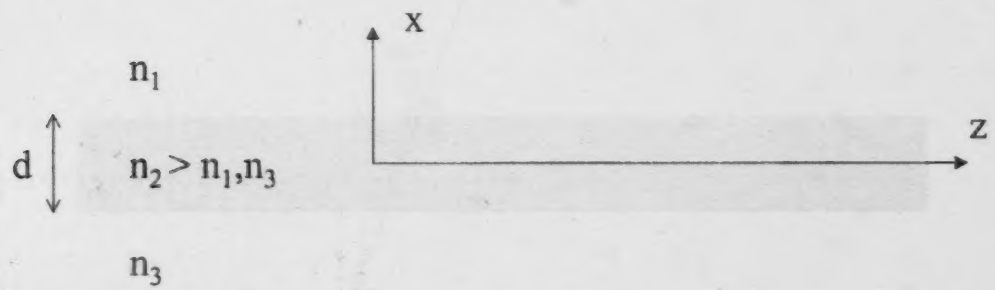

Figure 2.2.1 Slab waveguide. Cross sectional view of an idealized slab waveguide of thickness d. Each region is homogeneous, so that there is no variation in the y or z directions. In practice a slab waveguide is often grown on a substrate, so that it is often the case that $n_2 > n_3 > n_1$.

If we launch a plane wave in the z-direction, the slab waveguide appears like a potential well, and light can be confined. In a ray point of view, we picture the light bouncing off the boundaries and being trapped by total internal reflection (Fig. 2.2.2 top).

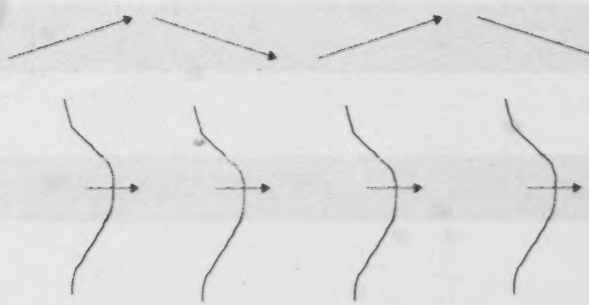

Figure 2.2.2 Waveguiding in slab. A slab confines light, allowing waveguiding. In the ray picture (top) reflection at the boundaries traps the light, while solution of Helmholtz equation leads to a modal view (bottom).

Wave behaviour dominates when the thickness of waveguide is reduced in thickness, and becomes of the same order as the wavelength of light. Here we turn to the Helmholtz equation to understand the system's behaviour. Anticipating the field will propagate in the z-direction, we use a solution of the form

$$E(x,z) = E(x)e^{-i\beta z}, \tag{2.2.2}$$

where β is the propagation constant of the wave in the z-direction. Splitting the total wave vector into a part in the z-direction (longitudinal or propagation wave vector, $\vec{\beta}$) and a part in the x-direction (transverse wave vector, $\vec{\kappa}$) we have[2]

$$\vec{k} = \vec{\kappa} + \vec{\beta}. \tag{2.2.3}$$

This relation is graphically illustrated in Fig. 2.2.3.

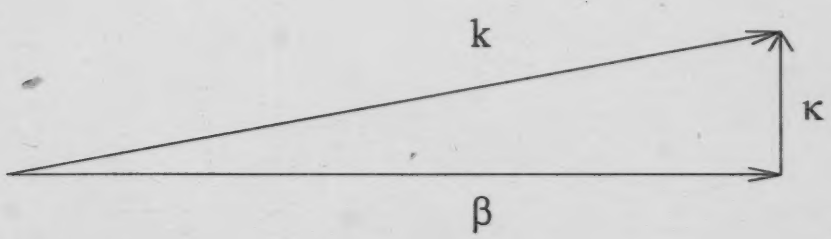

Figure 2.2.3 Wavevector in slab waveguide. When light is confined to a slab waveguide the total wave vector can be split into longitudinal, β, and transverse, κ, components.

The overall effect of a structure on the forward propagation of light can be described with a pseudo-index called the effective index N_{eff}

$$\beta = N_{eff} k_0, \tag{2.2.4}$$

[2] There is no change in the y-direction, leading to this dimension falling out of the equations.

allowing all material and structural effects to be lumped into the effective index.

Substitution of (2.2.2) into the Helmholtz equation results in the wave equation for slab waveguides

$$\nabla^2 \overline{E} + \left(k_0^2 n^2 - \beta^2\right)\overline{E} = \vec{0}. \qquad (2.2.5)$$

Second order differential equations have solutions with exponential/sinusoidal forms, suggesting the use of exponential test functions to solve for the allowed modes (solutions to the wave equation). On physical grounds the field profile is required to have finite energy, suggesting that the transverse field (exponentially) falls off outside the slab, while having (sinusoidal) oscillatory solutions within the slab itself.

Multiple transverse oscillatory solutions will occur as the thickness of the slab increases (as multiple half wave periods of the sinusoidal solution can exist). This condition is termed "multimodal", and is generally avoided[3].

Light can be polarized with the electric field either parallel to the slab surface (TE mode), or perpendicular to the surface (TM mode). This leads to both TE and TM solutions of the slab waveguide wave equation (2.2.5). The general features of these modes are the same, though TE modes are more strongly confined to the slab [14]. Often the TE mode is used in practice.

Once waves are confined to slab structures we can split them into longitudinal and transverse components. Within the core slab (transverse) oscillatory solutions exist, while outside the slab the field decreases exponentially (evanescent waves). The solutions to

[3] There are several reasons for preferring singlemode structures: Once energy is spread through several modes it can be difficult to place it back into a single mode (for example when coupling to optical fibres). Modeling becomes more difficult as interference effects become important. A lesser concern is intermodal dispersion, which limits data switching speeds (in integrated optics only small distances are traveled, reducing the importance of this effect, versus the case for fibres).

the wave equation, for a given structure, are called the (optical) modes. These modes can be shown to be orthogonal [14], which makes mathematical treatments much more tractable. The effective index allows the material and structural effects to be incorporated into a pseudo-refractive index, simplifying analysis of slabs.

2.3 The Transfer Matrix Method and the Slab Eigen-equation

In the previous section a qualitative description of slab waveguiding was given. In order to obtain a quantitative description it is useful to step back and reanalyze the slab, from the perspective of the transfer matrix method (TMM). The transfer matrix method is a powerful tool that provides a general framework for modeling slabs, allowing layered stacks of slabs to be treated. In the next section we will see how to use the effective index concept to model three-dimensional structures as a stack of slabs, enabling the transfer matrix method to be used to describe integrated optic devices.

For wave propagation in a one-dimensional homogeneous material (where the wave is only free to move on a single axis, which we will label as x) two counter propagating waves make up the possible solutions. For forward, E^+, and backward, E^-, fields the situation can be represented in matrix formalism to describe the effect of a material on light

$$\begin{bmatrix} E^+(x_2) \\ E^-(x_2) \end{bmatrix} = \begin{bmatrix} M_{11} & M_{12} \\ M_{21} & M_{22} \end{bmatrix} \begin{bmatrix} E^+(x_1) \\ E^-(x_1) \end{bmatrix}. \qquad (2.3.1)$$

In the case of free propagation a phase shift will occur after propagating a distance d

$$M_{region} = \begin{bmatrix} e^{i\beta d} & 0 \\ 0 & e^{-i\beta d} \end{bmatrix}. \qquad (2.3.2)$$

At an interface, with a discontinuous jump in the refractive index, Fresnel reflection will occur. For normal incidence this can be described as

$$M_{Interface} = \frac{1}{2n_i}\begin{bmatrix} n_i + n_{i+1} & n_i - n_{i+1} \\ n_i - n_{i+1} & n_i + n_{i+1} \end{bmatrix}, \tag{2.3.3}$$

where the interface is between two materials of refractive indices n_i and n_{i+1}. A schematic showing these situations is given in Fig. 2.3.1.

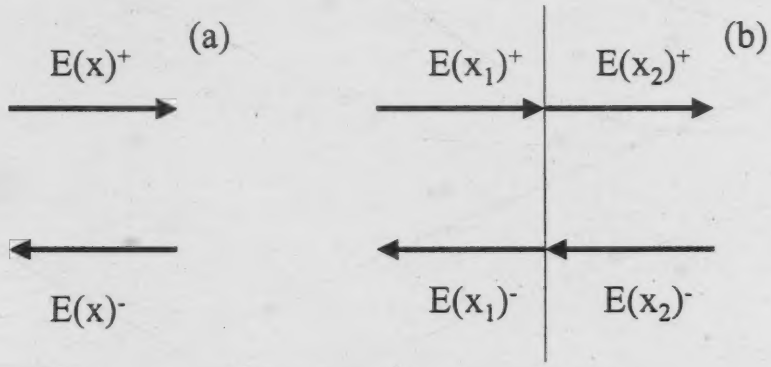

Figure 2.3.1 Wave propagation in homogeneous 1-D media. (a) Light can propagate either forward or backwards in bulk 1-D media, (b) at an interface reflection will occur, and energy will be redistributed into different modes.

To capture the effect of stacked slab regions the matrices of each subcomponent (the interfaces and homogeneous slab regions) can be multiplied together to find the matrix of the overall system. The ability to describe systems by multiplying matrices together allows the transfer matrix method to describe complex situations. Details of the transfer matrix method can be found [15] and [16].

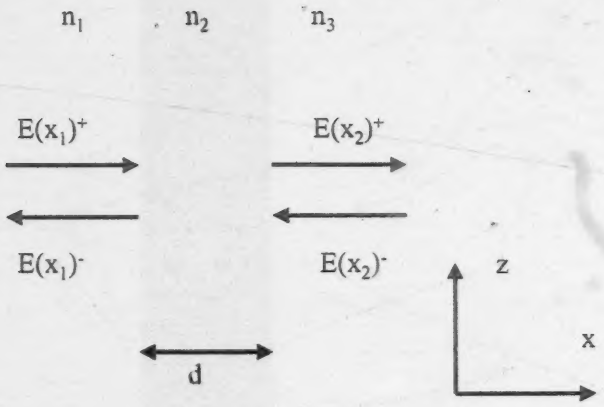

Figure 2.3.2 Slab Geometry. The transfer matrix method can be used to describe one-dimensional wave propagation. For waveguiding we require $E(x_1)^-$ and $E(x_2)^+$ to be zero (light does not leave the structure).

Considering a slab it is clear that for waveguiding no light can escape the structure, requiring $E(x_1)^-$ and $E(x_2)^+$ to be zero (see Fig. 2.3.2)

$$\begin{bmatrix} 0 \\ E^-(x_2) \end{bmatrix} = \begin{bmatrix} M_{11} & M_{12} \\ M_{21} & M_{22} \end{bmatrix} \begin{bmatrix} E^+(x_1) \\ 0 \end{bmatrix}. \tag{2.3.4}$$

For (2.3.4) to hold M_{11} must be equal to zero, allowing the condition for waveguiding to be found.

To find the waveguiding condition it is useful to introduce the q, h, p variables, which describe the component of the wave field perpendicular to a structure (i.e. the transverse wave component). The total wave vector is split between transverse and longitudinal components, giving

$$\kappa = \left[k^2 - \beta^2\right]^{\frac{1}{2}}. \tag{2.3.5}$$

Labeling the transverse components in the three regions (see Fig. 2.3.3) as q, h and p we have

$$q = \left[(n_1 k_0)^2 - \beta^2 \right]^{\frac{1}{2}}$$
$$h = \left[\beta^2 - (n_2 k_0)^2 \right]^{\frac{1}{2}} \quad . \tag{2.3.6}$$
$$p = \left[(n_3 k_0)^2 - \beta^2 \right]^{\frac{1}{2}}$$

For TE waves, M_{11} for the three-layer system can be shown to be [14]

$$M_{11} = \frac{1}{2}\left(1 + \frac{p}{q}\right)\cos(hd) - \frac{1}{2}\left\{\frac{h}{q} - \frac{p}{h}\right\}\sin(hd). \tag{2.3.7}$$

Equating this to zero (for confinement) results in the slab waveguide eigen-equation

$$\tan(hd) = \frac{h(p+q)}{(h^2 - pq)}. \tag{2.3.8}$$

Similarly for TM fields it can be shown [14] that the eigen-equation is

$$\tan(hd) = \frac{h(\tilde{p}+\tilde{q})}{(h^2 - \tilde{p}\tilde{q})}, \tag{2.3.9}$$

where $\tilde{p} = \left(\frac{n_2}{n_3}\right)p$ and $\tilde{q} = \left(\frac{n_2}{n_1}\right)q$.

The propagation constant must satisfy equation (2.3.8) (or (2.3.9) for TM modes) for guided waves. As these eigen-equations are transcendental, numerical solutions are required. For a given index profile (n_1, n_2, n_3) and the slab thickness d numerical solution of the eigen-equations results in allowed β values.

In integrated optics, thin films make up the basic building block for devices. This geometry is described by the slab waveguide, and we have seen that numerical solution is required. In the next section, we will see how to model three-dimensional structures as stacks of slabs, allowing the eigen-equation for the slab waveguide to approximately describe more complex devices.

2.4 The Effective Index Method

Using the idea of the effective index provides a technique for reducing the dimensionality of rectangular waveguide structures. This allows three-dimensional structures to be modeled as an equivalent slab system. The waveguide cross section is split into regions that are modeled as slab waveguides (regions I-III in Fig. 2.4.1). In each region an approximate β value is founding using the eigen-equation (2.3.8 or 2.3.9). From these β values effective indices are found for each region (2.2.4), resulting in a slab structure approximating the device. From this slab structure the eigen-equation can be solved to find the propagation constant for the waveguide.

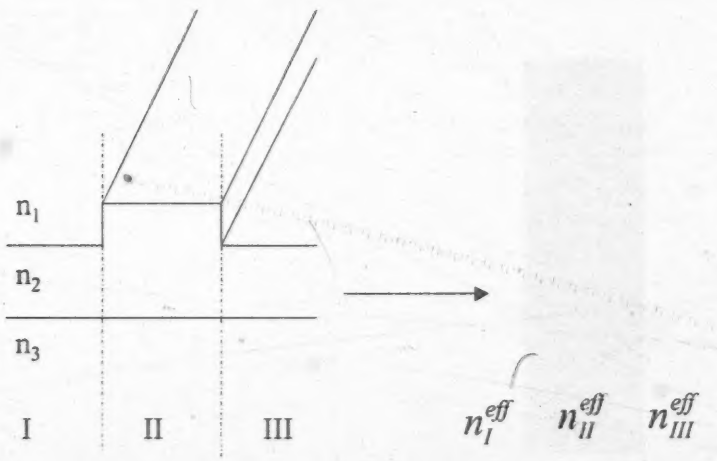

Figure 2.4.1 Schematic of the Effective Index Method. The cross section of the 3-D waveguide is split into slab waveguide regions and corresponding effective indices are found. Using these indices allows the 3-D structure to be represented by an equivalent 2-D system; a thin film slab replaces the 3-D structure.

There is a slight overestimation of the propagation constant, but overall this method gives good results [17], particularly relative to fabrication errors. The effective index method can be shown to be equivalent to a separation of variables solution of the wave equation, leading to the accuracy of the method [18]. The relation to separation of variables explains the tendency of the method to overestimate propagation constants (corner regions are only partially accounted for in the separation of variables approach, in the model the field is therefore more concentrated in the waveguide than in reality, as a result the propagation constant will be larger). It is notable that the slab structure will have interfaces with orientation perpendicular to the polarization in the physical structure, and care must be taken in selecting the appropriate slab eigen-equation.

Despite the fact this method is approximate, the simplicity of the approach combined with the existence of large fabrication errors and unknowns has led to its applicability and wide use.

2.5 Oversized Rib Waveguides

As a waveguide's cross section is increased it will eventually become multimoded. It is desirable to constrain the cross section of waveguides, allowing support of only one mode (singlemode). The characteristic scale that will support a mode is $\sim \frac{\lambda}{2n}$, which requires that small dimensions be used (~μm). The small dimensions used make it difficult to couple light between an optical fibre and a slab waveguide.

Oversized rib waveguide structures (Fig. 2.5.1) address these difficulties, allowing the construction of singlemode waveguide structures with cross sections up to an order of magnitude larger than traditional singlemode waveguides. For example, waveguides with 10 μm characteristic dimensions have been constructed for ~ 1 μm wavelength waves [19].

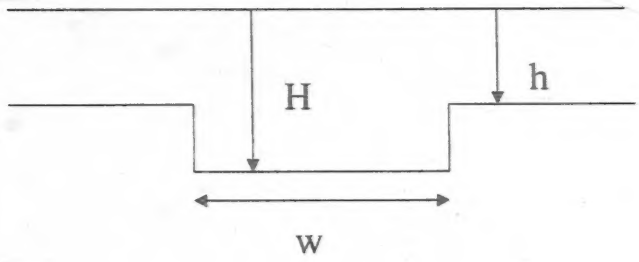

Figure 2.5.1: Cross Section of Inverted Rib Waveguide. Scaling the rib width (w), side slab height (h), and rib height (H) according to the oversized rib criteria allows single mode operation for large cross sections.

For singlemode operation of oversized ribs scaling rules on the rib width (w), side slab height (h), and rib height (H) exist [20]. As the rib structure is scaled up in size, higher order modes are supported. The scaling relations ensure that these modes are weakly bound. This allows the higher order modes to couple to modes in the side regions, resulting in these modes being radiated during propagation [20]. This effect is geometric in nature, reducing the dependence on wavelength and index of the guide. From the reported criteria, simplified conditions were found to be

$$H > h \geq \frac{H}{2}, \tag{2.5.1}$$

and

$$w < h. \tag{2.5.2}$$

Details of the derivation of this simplified criteria, and comparison to the original scaling rules reported in the literature, can be found in Appendix 1.

By using oversized rib waveguides, mode profiles similar to optical fibres can be achieved, improving the ability to couple light into integrated optic devices.

2.6 Directional Couplers

When two singlemode waveguides are in close proximity they form a composite structure that supports two modes, termed supermodes. The supermode picture is "laborious and does not submit itself readily to … intuitive understanding" [14], but is commonly described in reference texts [15]. As the (singlemode) waveguides in a directional coupler are brought into proximity, the two allowable single modes for the individual waveguides form into a symmetric and antisymmetric mode for the structure. These modes travel at speeds differing by the coupling strength between the guides. This introduces interference between the modes, causing energy to be transferred between the waveguides. This transfer of energy between waveguides is the operational feature of directional couplers.

As optical fields spill over from waveguides, one can imagine that the index profile seen by the fields confined by a singlemode waveguide starts to look like a large, multimoded, waveguide when another guide is brought close by. This perspective allows an intuitive grasp on why supermodes exist in a directional coupler.

Using the effective index method, directional couplers can be modeled as two high indexed slabs separated by a lower index slab (Fig. 2.6.1). In the design of directional couplers, it is critical to keep waveguide separations on the order of the waveguide widths, both to keep device lengths small and to minimize the error introduced by the effective index method. It is found that error increases from a few percent for separations below the width of the waveguides to over 20% as separation increases beyond the waveguide width [21]. As fabrication resolution is relatively large (~ 0.5 μm for contact printing [22]), error introduced by the effective index method is comparably insignificant for "small" waveguide separations.

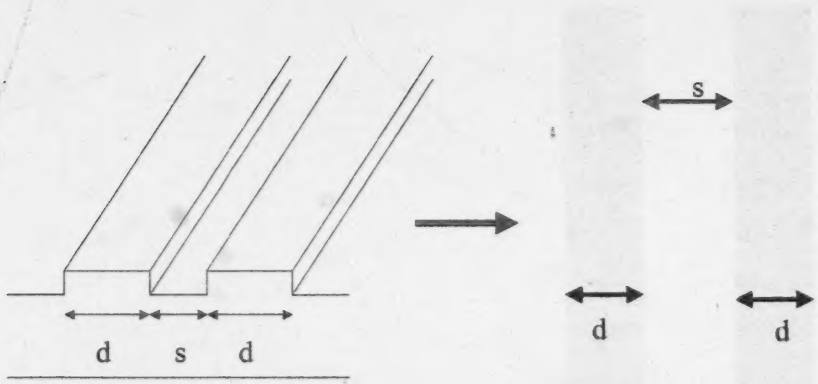

Figure 2.6.1: Effective index model of a directional coupler. Waveguides of width d separated by a distance s can be modeled as a stack of slabs.

Coupled mode theory (CMT) allows for an alternative description of the directional coupler. In coupled mode theory small perturbations to the refractive index are accounted for, and used to solve the Helmholtz equation. The refractive index profile of the unperturbed structure is modified by the perturbations, such that

$$n^2 \to (n+\Delta n)^2. \tag{2.6.1}$$

The modes of the original waveguides make up the solution, but with dependence on the propagation direction now assumed.

For the case of two waveguides in close proximity the mode from one waveguide will overlap the second waveguide. The fields will therefore see a perturbation; solution of this case can be found in reference texts (see, for example, [23]). For identical, linear, waveguides complete power transfer will occur, and energy will "slosh" between the waveguides along the z-direction. The normalized light intensities in the two coupled waveguides follow the relationship [23]

$$\begin{aligned} I_1(z) &= \cos^2(\kappa_C z) \\ I_2(z) &= \sin^2(\kappa_C z) \end{aligned}, \tag{2.6.2}$$

where the coupling term κ_c measures the strength of the coupling between the waveguides.

The coupling coefficient contains the effect of the device structure, and is therefore useful for modeling. Various approximations of the coupling coefficient can be found. For the equivalent slab geometry (Fig. 2.6.1) the coupling coefficient is given in [24]. As we wish to design for TE polarized light we must use the TM equations for the slab system. The expression is fairly complex, but follows the basic form

$$\kappa_c \propto \frac{e^{-s}}{d}, \tag{2.6.3}$$

where s is the spacing between the waveguides, and d is the width of the waveguides. There is an exponential dependence on the waveguide spacing, due to the evanescent drop off of the waveguide modes. This is a source of difficulty in successful fabrication of operational directional couplers.

Yariv has performed an analysis combining the use of the coupled mode and supermode views, allowing calculation of the supermode propagation constants from the coupling coefficients [14]. A sketch of this analysis is repeated here, as it provides a good understanding of the directional coupler.

The modes in the waveguides can be represented as

$$\bar{E}(z) = \begin{bmatrix} E_1(z) \\ E_2(z) \end{bmatrix}, \tag{2.6.4}$$

where E_1 and E_2 represent the modes in the first and second waveguides. During propagation the fields will evolve, due to coupling, as

$$\frac{\partial \bar{E}}{\partial z} = \begin{bmatrix} -i\beta & -\kappa_c \\ \kappa_c & -i\beta \end{bmatrix} \bar{E}, \tag{2.6.5}$$

for the case of identical waveguides. This coupled mode view is now reinterpreted from the perspective of supermodes. Supermodes are stable modes, and therefore can only have phase changes during propagation, requiring a solution of the form

$$\bar{E}(z) = \bar{E}(0) e^{i\tilde{\beta}_{1,2} z}, \tag{2.6.6}$$

where $\tilde{\beta}_{1,2}$ are the propagation constants of the supermodes. Substitution of (2.6.6) into (2.6.5) results in

$$i\tilde{\beta}_{1,2} \bar{E} = \begin{bmatrix} -i\beta & -\kappa_c \\ \kappa_c & -i\beta \end{bmatrix} \bar{E}. \tag{2.6.7}$$

Solving (2.6.7) leads to

$$\tilde{\beta}_{1,2} = \beta \pm \kappa_c. \tag{2.6.8}$$

Yariv's analysis demonstrates that supermode propagation constants are related to the coupling coefficient in a simple way. This allows supermodes to be calculated by using the effective index concept and known expressions for the coupling coefficient

$$\tilde{\beta}_{1,2} = N_{1,2}^{eff} k_0 = \beta \pm \kappa_c, \tag{2.6.9}$$

so that the effective refractive indices, as seen by the supermodes, are

$$N_{1,2}^{eff} = \frac{\beta \pm \kappa_c}{k_0}. \tag{2.6.10}$$

In summary, directional couplers, consisting of two waveguides in close proximity, can be modeled as coupled slab waveguides. As the waveguides become close enough for the waveguide modes to overlap the structure becomes multimoded, where the allowed modes are termed supermodes. Coupled mode theory is a perturbation method that allows for estimation of the coupling between modes, due to modifications in the refractive index profile. The propagation constant of the supermodes can be calculated from the coupling coefficient, as estimated by coupled mode theory.

2.7 Gratings

Periodic variations (gratings) in a waveguide may cause reflection. Considering a sinusoidal grating, with a period Λ and a magnitude δn, the perturbation is

$$\Delta n = \delta n \sin\left(\frac{2\pi}{\Lambda} z\right), \tag{2.7.1}$$

so that

$$n^2 \rightarrow \left(n + \delta n \sin\left(\frac{2\pi}{\Lambda} z\right)\right)^2. \tag{2.7.2}$$

For weak gratings δn is small, allowing the following approximation

$$n^2 \rightarrow n^2 + 2n\delta n \sin\left(\frac{2\pi}{\Lambda} z\right). \tag{2.7.3}$$

Substituting this into the wave equation gives

$$\nabla \vec{E} + \left[k_0^2 n^2 + k_0^2 2n\delta n \sin\left(\frac{2\pi}{\Lambda} z\right)\right]\vec{E} = 0. \tag{2.7.4}$$

Under the assumption that the grating is weak we expect the electric field to consist of modes of the unperturbed structure

$$\overline{E} \sim e^{i\beta z} + e^{-i\beta z}. \tag{2.7.5}$$

Substituting (2.7.5) into the wave equation for the structure (2.7.4) leads to a perturbation term, induced by the grating structure, of

$$\Delta \sim \sin\left(\frac{2\pi}{\Lambda} z\right)\left(e^{i\beta z} + e^{-i\beta z}\right). \tag{2.7.6}$$

Assuming that this term is only important if its average effect is sizeable, we first multiply by $e^{-i\beta z}$ (which is allowed, as the other side of equation (2.7.4) is equal to zero) to eliminate one term (after averaging). This leads to

$$\langle \Delta \rangle \sim \left\langle \sin\left(\frac{2\pi}{\Lambda} z\right) e^{-i2\beta z} \right\rangle. \tag{2.7.7}$$

Using the exponential representation for the sin term in (2.7.7), and considering its real component, reveals that the perturbation term will be near its maximum when

$$\beta \simeq \frac{\pi}{\Lambda}. \tag{2.7.8}$$

A grating will therefore have wavelength dependent reflection, allowing for wavelength selection. The wavelength satisfying (2.7.8) is termed the Bragg wavelength of the grating.

Detailed analysis of sinusoidal gratings using the coupled mode theory can be found in many textbooks (see for example [23]), where estimates on the magnitude of the reflection and other quantities are derived. A useful finding is that sinusoidal and periodic slab grating profiles (of the same period) are equivalent, up to proportionality constant [23]. This allows the use of the transfer matrix method to model sinusoidal gratings. Conceptually this can be understood, as the Fourier expansion of a slab grating profile will consist of sinusoidal terms of increasing order. The first order term will have the same period as the slab stack, and dictates the fundamental bandgap.

When (2.7.8) is satisfied the grating coupling coefficient, κ_g, can be found from coupled mode theory to be [14]

$$\kappa_g \approx \frac{2\delta n}{\lambda}. \qquad (2.7.9)$$

The effect of the grating on light is therefore directly proportional to the refractive index perturbation, and is strongly wavelength dependent.

The right hand side of (2.7.9) can be multiplied by an integer m, for a m^{th}-order grating (a grating scaled up in size by m-times); though care must be taken here. This condition determines when reflection occurs, and interference effects must be considered. Modeling a sinusoidal grating as a periodic stack of slabs we can find two general classes of m^{th} order gratings. The thickness of each slab is the same, and as the index perturbation is small, we can consider the limiting case where the optical thickness of each slab is identical. We immediately realize that two extreme cases can occur – that of total constructive interference of the light reflected at each slab boundary, and that of total *destructive* interference. These limiting cases correspond to quarter-wave, and half-wave, stacks [15]. When m is an odd integer constructive interference will occur, and the grating will cause strong reflection at the Bragg wavelength; for even order gratings only weak reflection will occur. Therefore only odd order gratings should be used when reflection is required.

In summary, the wave equation for homogeneous media was introduced, and modified for slab waveguides. Gratings (periodic variation in refractive index) cause wavelength dependent reflection. Sinusoidal gratings are obtainable by holographic formation, and can be modeled using the transfer matrix method.

With the elements introduced in this chapter design and simulation of grating-assisted add-drop filters can performed, and this is discussed in the next chapter.

3. Design of Grating-Assisted Add-Drop Filters[1]

A directional coupler composed of two identical waveguides and imprinted with a grating acts as an optical filter for wavelength routed networks (Fig. 3.1). Away from the Bragg wavelength the optical signals pass through the device, while at the Bragg wavelength the grating section L_2 acts as a distributed mirror, allowing signals to be added to or dropped from a wavelength routed network. For symmetric add and drop characteristics, the end regions, L_1 and L_3, are set equal.

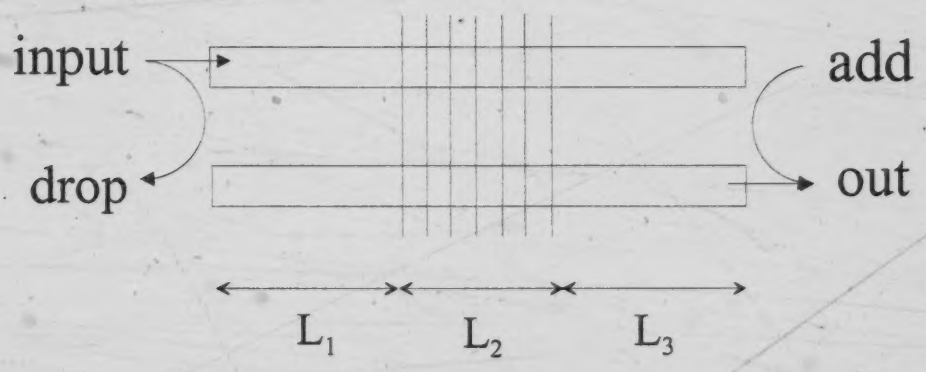

Figure 3.1 Grating assisted add-drop filter. Two waveguides in close proximity will transfer energy between them. Plaeing a grating in the mid region will cause wavelength selective reflection. By making the structure physically symmetric, identical add-drop characteristics result.

The embedded Bragg grating provides the wavelength selectivity of grating-assisted filters. The required first-order grating period Λ is (2.7.8)

$$\Lambda = \frac{\pi}{\beta_{Bragg}}, \qquad (3.1)$$

[1] A version of this chapter has been published. R. M. Bryce, R. G. DeCorby, C. Haugen, Y. Y. Tsui, and J. N. McMullin, "Grating assisted optical add drop filter modeling and fabrication", Proceedings of the International Conference on Applications of Photonic Technology (Photonics North), IEEE/SPIE, Quebec City, June 2-6, 2002.

where β_{Bragg} is the Bragg propagation constant in the waveguide, equal to $2\pi n_{eff}/\lambda_{Bragg}$. λ_{Bragg} is the wavelength to be filtered, and n_{eff} is the model effective index. To first order n_{eff} is the refractive index n of the waveguide core. For possible values of n (ranging from ~1 to ~ 4 for typical materials [15]) Λ is of the order of 0.5 μm for λ_{Bragg} = 1.55 μm, representative of a wavelength channel in optical networking.

To reduce complexity, we convert the 3-dimensional inverted rib coupler into an equivalent slab system, via the effective index method. This approximation has been demonstrated to be good far from cut-off for many devices; and in particular for directional couplers with gratings by Weber [25], who compared the approximation to full vectorial finite-element simulations.

As we wish to design for TE polarized light we must use the TM equations for the slab system, and the appropriate equation given in [24] (with the basic form described in (2.6.3)) is used to describe the coupling between the waveguides. The effect of the grating is modeled using the coupling coefficient of a grating (2.7.9).

The coupling parameters describe the device parameter space, and it is useful to find design equations based on these variables.

3.1 Design Equations

The theory introduced in the previous chapter allows the behaviour of structures to be determined. The ability to determine the structure from required behaviour is desirable, as this guides design. Using the results from coupled mode theory allow the formation of design equations, allowing suitable add-drop optical filter structures to be found.

Along the propagation direction z, the normalized light intensities in the two coupled waveguides follow the relationship (2.6.2)

$$I_1(z) = \cos^2(\kappa_C z)$$
$$I_2(z) = \sin^2(\kappa_C z) \qquad (3.1.1)$$

For an added or dropped signal at λ_{Bragg}, the distance traveled will be $2L_1$, due to reflection off the grating, plus a penetration into the grating (see Fig. 3.1). This penetration into the grating can be accounted for by a phase shift $\delta\varphi$ imparted. We want no energy reflected back into the input port and 100% add/drop of the Bragg wavelength. This requires the argument in (3.1.1) be $\pi/2$

$$\kappa_c 2L_1 + \delta\varphi = \frac{\pi}{2}. \qquad (3.1.2)$$

For the wavelengths to be passed through the device we set $z = L_T$, where L_T is the total device length ($L_T = L_1 + L_2 + L_3 = 2L_1 + L_2$). In order to tune the length of the grating to ensure[2] $|\kappa_g|L_2>3$, to fully reflect the add-drop signal [26], the argument in (3.1.1) is some multiple (typically m>1) of $\pi/2$

$$\kappa_C L_T = \kappa_C(2L_1 + L_2) = m\frac{\pi}{2}. \qquad (3.1.2)$$

Solving (3.1.1) and (3.1.2) for the lengths results in

$$L_1 = \frac{\pi}{4\kappa_c} - \frac{\delta\varphi}{2\kappa_c}$$
$$L_2 = (m-1)\frac{\pi}{2\kappa_c} + \frac{\delta\varphi}{\kappa_g} \qquad (3.1.3)$$

[2] While somewhat arbitrary, the relationship $|\kappa_g|L_2>3$ is simple to remember and forms a rule of thumb often used in practice.

As $|\kappa_c| < |\kappa_g|$ is necessary for proper operation of the filter[3] [27] we can estimate the phase shift using [26]

$$\delta\varphi \cong \tan^{-1}\left(\frac{\kappa_c}{|\kappa_g|}\right) \cong \frac{\kappa_c}{|\kappa_g|}. \tag{3.1.4}$$

Substituting this back into (3.1.3) we obtain the following design equations

$$\begin{aligned} L_1 &= \frac{\pi}{4\kappa_c} - \frac{1}{2|\kappa_g|} \\ L_2 &= (m-1)\frac{\pi}{2\kappa_c} + \frac{1}{|\kappa_g|} \end{aligned} \tag{3.1.5}$$

These design equations are found to be identical to those obtained by Ofusa *et al.* [28], who used equations developed by Baumann and Nowak using microwave s-parameter analysis [29].

3.2 Sensitivity Analysis of Design Equations

Sensitivity analysis attempts to quantify the stability of a device against environmental factors. The inputs and parameters of a system are perturbed and the change in the output or operation of the device is measured. This simple idea allows the important factors to be quickly found, and captures a sense of the robustness of the device. Very sensitive systems are difficult to work with, as small uncertainties and noise will have profound effects on the final result.

Fabrication errors in the device parameters can be investigated by finding the corresponding perturbation in the coupling coefficients and observing how L_1 in the

[3] As coupling between the waveguides increases there is an associated increase between supermode propagation constants (2.6.8). Eventually equation (3.1) will no longer be satisfied for both modes.

design equations (3.1.5) would have to compensate for effective adding/dropping of the Bragg wavelength. Modification of the parameters demonstrates that, as expected, waveguide spacing is critical (Fig. 3.2.1, top).

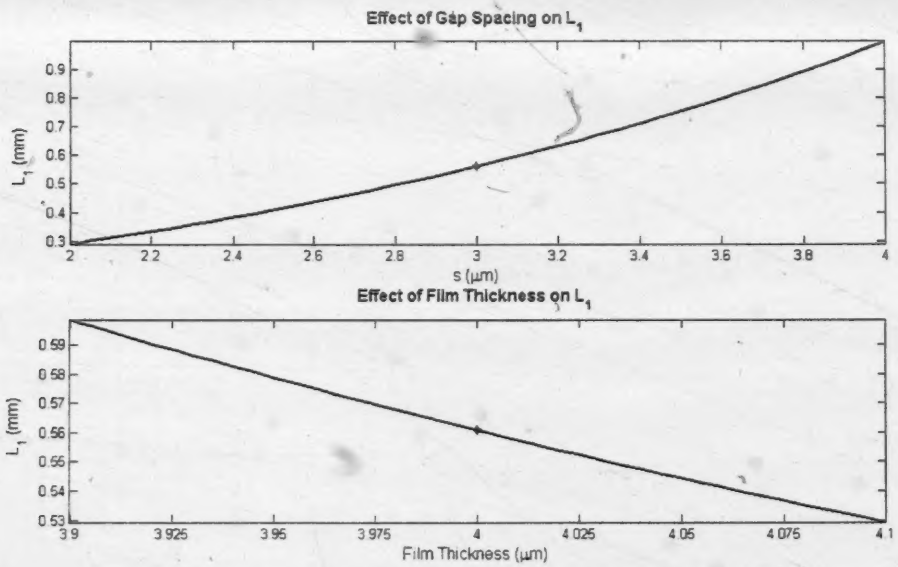

Figure 3.2.1: Sensitivity on waveguide spacing and film thickness. Note that these effects are of approximately equal strength.

Film thickness was also found to be critical (Fig. 3.2.1, bottom). This can be understood, as the effective index between the guides will approach the core index as the film thickness increases, causing the mode profiles to extend more and thereby increasing coupling. The film thickness can therefore be used as a tuning parameter to compensate for errors in the spacing of fabricated waveguides. This ability to counteract the hypersensitive dependence on waveguide spacing is crucial for fabrication within a single mask cycle (as features are modified during lithographic transfer from a mask, in a process dependent manner). Correcting for spacing error offers a practical means to achieve operational directional couplers, and directional coupler based devices, as film thickness is highly controllable.

3.3 Transfer Matrix Simulations

The design equations described in Section 3.1 allow device parameters to be readily selected, but give little insight into filter characteristics. In order to obtain filter characteristics for device optimization the transfer matrix method was used.

Using a three-step method of

(1) reducing of the 3-dimensional structure into an equivalent slab system (effective index method),

(2) finding the supermodes of the system (2.6.10), and

(3) propagating the modes through the structure (TMM),

the transmission and reflection characteristics of various ports can be simulated[4]. In finding the supermodes, the grating is treated as having a square profile. The simulation did not take overlap integrals (mode coupling loss) into account, but can be modified to do so [25]. The filter bandwidth is proportional to δn, which is tunable via modification of photodarkening exposure dosage.

Typical simulation results are displayed in Fig. 3.3.1, details of the structure can be found in Table 3.5.1 and the refractive index of the chalcogenide is described in (3.5.1).

Ringing is observed outside of the selected band, due to sudden truncation of gratings (in general this effect is known as Gibb's phenomena, and occurs when waves sample discontinuities). In k-space, this sudden truncation corresponds to a sinc profile modulation of the grating effect. This can be reduced by physically modulating the grating with a Gaussian profile, which results in a smoother frequency response (less ringing, see Fig. 3.3.2 and 3.3.3).

[4] Simulations were done with MatLab code designed by R. G. DeCorby, after [16].

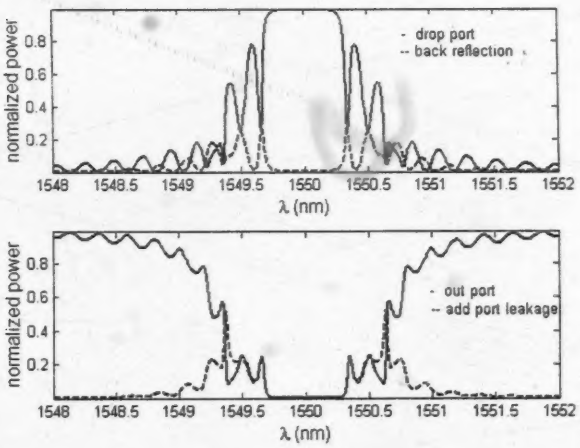

Figure 3.3.1: Transfer Matrix Method simulation of grating assisted filter. A drop wavelength of 1.55 μm was selected. Note the flat "top hat" response near this wavelength, and the ringing at the edges of the selected band.

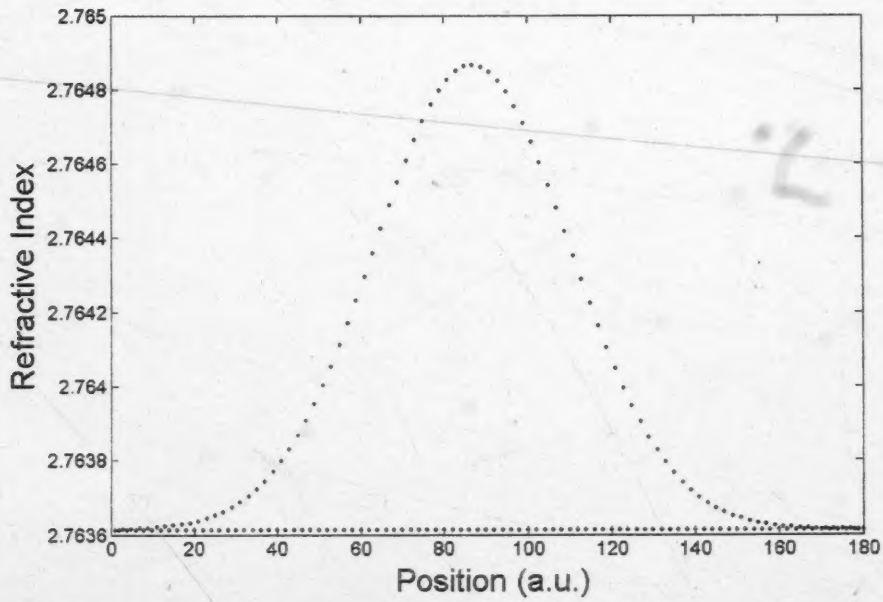

Figure 3.3.2: Gaussian grating profile. Varying a grating with a Gaussian envelope can be used to suppress "ringing", and thereby reduce cross-talk into adjacent channels. Here an exaggerated profile is shown to illustrate the modulation. The data points correspond to grating high and low regions, alternating between "zero" (background index) and a Gaussian modulated high index value.

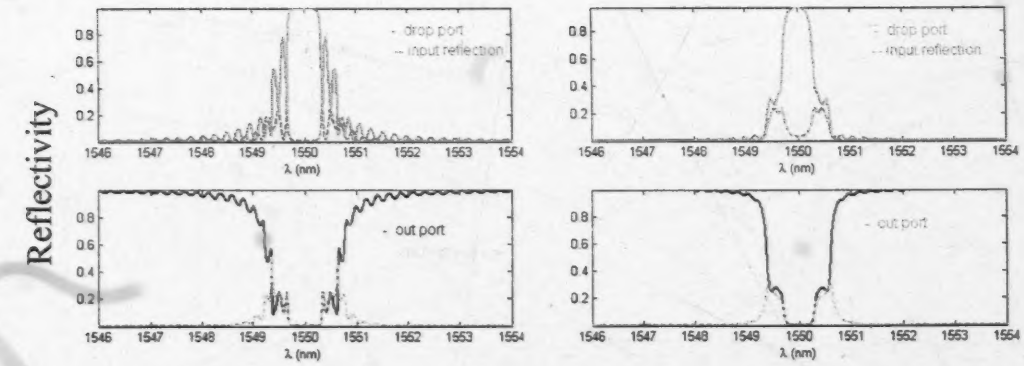

Figure 3.3.3: Effect of Gaussian grating profile. Ringing is induced by sudden truncation of gratings (left image), by varying the grating within a Gaussian envelope the ringing can be reduced (right image).

3.4 Fan Out Tapering

The waveguides in a directional coupler are ~ 10-100X closer together than the minimal separation possible between optical fibre cores, requiring the waveguides to be tapered away from each other to accommodate fibre coupling. For symmetric devices the energy distribution between modes smoothly transfers during the transition from isolated waveguides to the coupled system [25]. When adiabatically tapering one therefore only has to track the relative phase between the modes. Ensuring that the phase experienced between supermodes, in the tapered case, is equal to the linear case should result in identical performance (to the first order).

To simplify design and fabrication considerations, only the non-grating regions are modified (sections L_1 and L_3 in Fig. 3.1). We therefore change L_1 and L_3 from linear segments into out-curving tapers under the condition

$$\int \kappa_c(s)dl = \kappa_c(s_0)L_1, \qquad (3.4.1)$$

where the integration is over the length of the proposed taper section, $\kappa_c(s)$ is the coupling coefficient of the differential segment in the (now curved) end region at the separation s, and s_0 is the spacing of the waveguides in the original design. In other words, the phase experienced between supermodes in the tapered section (left hand side of (3.4.1)) is kept equal to the phase experienced in the linear case (right hand side of (3.4.1)). In practice, the end separation of the waveguides should be set so the filter can be butt-coupled to standard V-Groove chips (250 μm pitch), and this separation value was used.

Since wave fields are bound *to* a waveguide and not confined within it, light is lost during waveguide bends. Therefore required bend radii can be as large as millimeter ordered to prevent dramatic light loss, for low confinement waveguides. This effect can be understood as follows: light will be lost in the region outside the waveguide when the propagation speed required to remain in the wavefront becomes greater than the speed of light in the medium, resulting in the light radiating away. Waveguide bends are thus critical elements, and many designs to optimize bends exist. Cosine s-curves are a good configuration to connect laterally offset waveguides, as they are relatively easy to design and fabricate while providing a low-loss transition [30], and have been used in the design. The equation describing a cosine s-curve is given as

$$s(z) = \frac{h}{2}\left[1 - \cos\left(\frac{\pi z}{L}\right)\right], \qquad (3.4.2)$$

were s is the waveguide separation, h is the vertical offset experience by the waveguide, and L is the length over which this offset occurs.

Analysis with the beam propagation method (BPM) (Fig. 3.4.1) of designed directional couplers indicates that equation (3.4.1) is valid, allowing simple design. A commercial package, Prometheus, was used here, but due to instability in the software another package, OptiBPM, was selected for mask design and as a final verification of device structures.

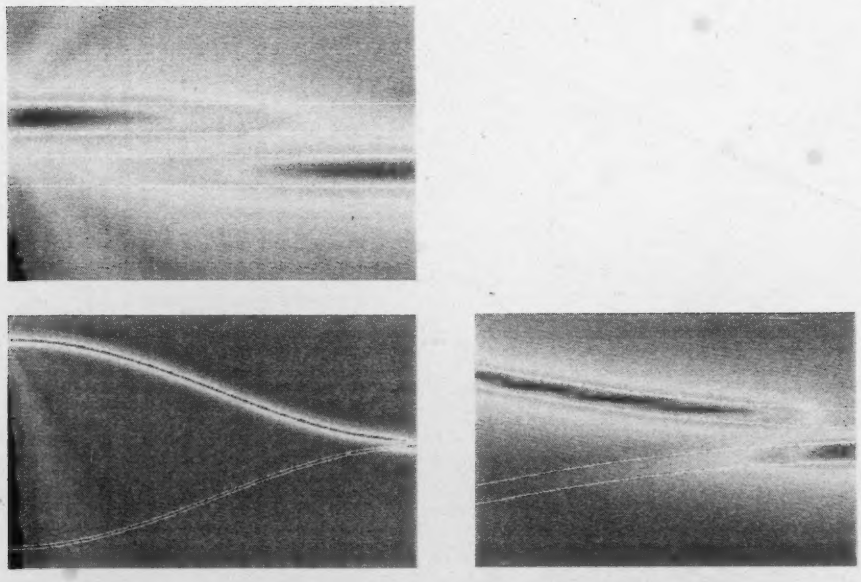

Figure 3.4.1: Beam propagation verification of taper methodology. A linear directional coupler with 100% power transfer between waveguides was designed (top), a tapered equivalent structure was found keeping phase shift experienced between supermodes equal. BPM analysis on the tapered section (bottom) was performed, where it can be seen that power transfers between waveguides (the bottom right image is a close up of the end region of the bottom left hand image). The waveguide structure is outlined in gold, and the optical power is in false colour scale (blue – low power, red – high power).

To provide uniformity between designed devices, the length of the s-bend was set equal for all devices (5000 μm), where BPM calculation indicates that < 1 % of power was lost due to bending radiation. Equation (3.4.1) is therefore modified so that the phase experienced in the linear case must be equal to the phase in the s-bend plus a linear element.

3.5 Mask Design for Devices

Devices were designed with the equations found, and a mask was fabricated with 4 μm wide waveguides for an inverted rib waveguide of 4 μm thick rib section, 3 μm thick side

sections, and variable waveguide separation in the coupling region[5]. Waveguide separations of 3, 4, and 5 μm for m=2 devices (3.1.5), as well as 3 and 4 μm for m=3 devices, were used. The refractive index of the chalcogenide glass was not completely known at the time of mask design, so several different indices were used. The index of films was assumed to follow

$$n(\lambda) = \sqrt{\frac{A}{\lambda^x} + B}\,, \tag{3.5.1}$$

where the parameters A, B, x were fit from data obtained with Swanepoel's method (see Appendix 2), from 0.7 μm films deposited by a collaborating group (S.O. Kasap *et al.*, U of S[6]) in the range of 700 nm to 1800 nm, and found to be A = 1.452e-19, B = 7.534, and x =3.1 [31]. Modifications of plus and minus 0.001, and 0.005, account for possible index perturbations between deposited films, as well as effects of using different substrate materials on effective indices (silica substrates were assumed, to guide design).

Grating lengths were set using different values for κ_g. Saliminia *et al.* [32] found a first order grating coupling coefficient of 403.3 and an effective second order[7] coupling coefficient of 454.6, for holographic gratings formed by argon ion laser in chalcogenide glass films. In general, we expect index perturbations of 0.00P to induce coupling coefficients around P thousand, per m^{-1} (for ~ 1 μm wavelengths, see (2.7.9)), so a reasonable set of grating coefficient values to design for is [2500, 2000, 1000, 800, 400], as an index modulation in the grating of 0.0025 results in a drop bandwidth of ~ 0.08 nm

[5] The device is defined by overlaying gratings on a directional coupler. It was found that positioning of the grating is stable against large placement error. Sensitivity analysis indicates that even 50 μm perturbation in the grating location has minimal effect (~ few percent) on device performance. Therefore only the directional coupler mask needs to be precise and alignment criteria are reduced. Design was thus focused on creating a high quality mask with directional couplers and alignment marks, for aligning a mask to define gratings.

[6] See http://www.usask.ca/crc/profiles/kasap.php for contact information.

[7] As mentioned in Section 2.7 second order sinusoidal gratings should not result in strong reflection. Here it is likely that the photodarkening process saturated, resulting in a non-sinusoidal grating. It is noted that general grating profiles are difficult to model. As the exact profile of a saturated photodarkened grating would be difficult to measure, and grating behaviour is highly dependent on this profile, care should be taken to prevent saturation.

(the standard WDM channel spacing set by the International Telecommunications Union). These values were used in device design; see Table 3.5.1 for representative device parameters.

Table 3.5.1 Representative device parameters. For 1.55 μm wavelength the design equations found result in devices with parameters of this order.

n_0	2.772	s	3 μm
δn	0.0025	Λ	280 nm
w	4 μm	m	2
H	4 μm	L_1	0.5609 mm
h	3 μm	L_2	1.740 mm

Substrates of standard 4" oxide coated Si wafers were assumed for design. To ensure features are on the wafer in useable regions, the mask file was designed to be 10 by 10 cm and the devices were centered on the middle 6 by 5 cm region for easier handling and processing. The devices are 254 μm by about 2 cm in size, including taper sections. Giving each device 2 mm vertical and 3 cm horizontal span to allow for the device spacing and alignment marks enables 50 devices to be created. 25 devices were designed, and were duplicated in order to protect against processing errors. Outside of this region linear waveguides and oversized alignment boxes where placed to allow for testing and to facilitate mask-wafer alignment. In addition, a pattern was placed by each device, to allow for identification of devices after dicing. See Figure 3.5.1 for the mask layout.

A generalized layout script was created to position devices for the mask blueprint, and alignment marks were positioned around the devices. This allowed rapid modification of design, and reduces the difficulty of verification and modification, by placing menial calculation demands on the computer. Each device was summarized in an object data structure, containing the relevant parameters (waveguide separation, taper lengths, linear

device lengths, and order of device). This abstraction step allows important design parameters to be manipulated, without having to explicitly manage the required details.

OptiBPM was used to verify designed structures operated correctly; design and numerical predictions were within 10% of each other. The design values were used to define the mask, due to time constraints preventing numerical optimization for each device (an evaluation version of the OptiBPM software with a timed key was used).

Design equations were found for grating assisted add-drop filters, for linear waveguides in close proximity. A method to guide tapering of the waveguides, to allow coupling to optical fibres, was proposed and verified using numerical simulations. A mask was designed, and was fabricated by Adtek Photomask.

The next chapter investigates process development and fabrication issues.

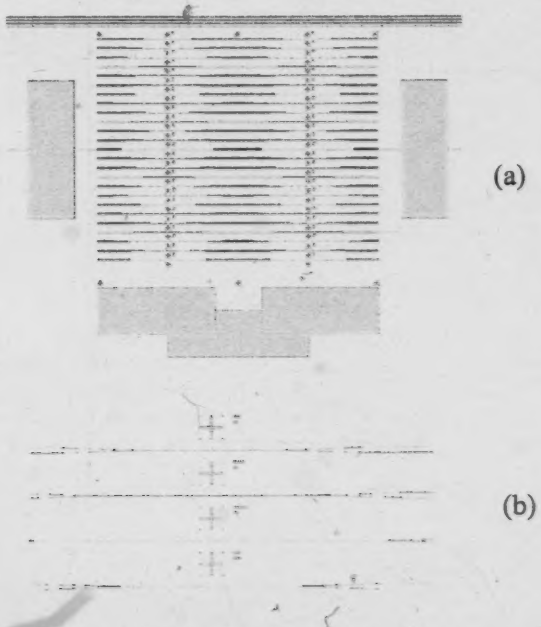

Figure 3.5.1: Mask Layout. The mask consists of 25 directional coupler based devices, which are duplicated to make 50 device structures. In (a) the directional couplers can be seen in the center of the layout area. Large boxes are located on the left and right edges and the bottom, in order to facilitate alignment. Linear waveguides are located across the top of the layout, in order to allow testing. In (b) a magnified section showing detail of the directional couplers is shown. Alignment marks, and the patterns for device identification can be seen.

4. Process Development

Well-confined waveguides are insensitive to slight modification in substrate index, and numerical studies on the oversized rib waveguides designed demonstrate that a 0.1 change in the substrate index modifies the waveguides effective index by ~ 0.001. This stability against modifications in the substrate index allows the mask (designed for oxide substrates) to be applied to a wide variety of other substrates allowing polymers to be used, as well as oxide.

4.1 Robust Polymer Undercladding[1]

Chalcogenide glass exhibits large thermal expansion, often leading to cracking under annealing conditions. Polymer films have thermal expansion coefficients larger than most technologically important optical materials [33], indicating that damage due to differences in thermal expansion can be reduced by their use as an undercladding. In addition polymers tend to adhere well to a variety of substrates and are easily processed, making them candidates for use with chalcogenide glass.

A disadvantage of polymers, for use in thin films, is questionable thermal stability. Many polymers used in thin films have low glass transition temperatures, potentially leading to structural modification and material flow during processing, as well as long-term stability concerns. For this reason high temperature glass transition polymers have been investigated. Solvay Advanced Polymers supplied sulfone and polyamide-imide polymers for investigation, both of which have high glass transition temperatures and are mechanically strong. Glass transition temperatures of 190 °C for polysulfone, 220 °C for polyethersulfone, and 280 °C for polyamide-imide indicate these polymers are suitable for use with As-S-Se chalcogenides, which have $T_g \approx 200$ °C

[1] A version of this section has been submitted for publication. R. M. Bryce, H. Nguyen, P. Nakeeran, T. Clement, C. J. Haugen, R. Tykwinski, R. G. DeCorby, and J. N. McMullin, "Polyamide-imide thin films for integrated optics", Thin Solid Films.

Sulfone polymers contain a sulfur link in their backbone. These polymers are widely used in membranes used for separation and purification of fluids, due to their mechanical strength and resistance to degradation.

To prepare sulfone polymers for use polyethersulfone (Radel A, Solvay) and polysulfone (Udel, Solvay) were dissolved in N,N-Dimethylacetamide (DMAC) solvent at a ratio of 1 g of polymer to 5 mL of solvent[2]. This solution was filtered to remove impurities and spun cast on silicon and oxide coated silicon wafers. The solution was spread over wafers, and spun at 300 rpm for 20 s followed by a 600 rpm spin for 30 s to establish uniform thin films. After spinning the films were cured at 80 °C to harden the films. Polyethersulfone films were measured to be nominally 6 μm thick; polysulfone films had a nominal thickness of 8 μm. High quality films which passed the scotch tape test were obtained, but large losses where measured at 633 nm and films cracked when exposed to acetone (commonly used in lithography). Effort was focused on polyamide-amide films which where found to be more resistant to chemicals.

Polyamide-imide (PAI) polymer (Torlon AI-10, Solvay) has excellent thermal [34], mechanical [35], and chemical [36] stability, and possesses good processibility (melt-processable and injection moldable, as well as machinable). Its stability indicates that films and devices will be rugged, resisting damage during processing and in use. Torlon (PAI) is similar to polyimide (PI), which is commonly used in integrated optic devices [2] and MEMS [37]. As Torlon is well characterized [36], robust, and similar to PI, its optical properties and potential as a material for integrated optics was investigated.

To prepare Torlon for spinning, a solution was made using N, N-dimethyl formamide (DMF) as a solvent, with a concentration of 60 grams of Torlon in 150 mL of DMF. Once made the solution was filtered with 1 μm particle retention paper. Si, SiO_2 coated Si, quartz, and borofloat glass wafers were used as substrates, and in some cases BCB

[2] N,N-dimethylformamide, quinoline, chlorobenzene, cyclopentane, and methylene chloride solvents were also used, but films either failed to form or had poor quality.

polymer [38] was used as an undercladding material. The wafers were cleaned in a standard piranha solution (3:1 sulfuric acid : hydrogen peroxide) for 15 minutes, rinsed, and baked at 120° C for half an hour to drive off moisture. Torlon was spun cast on wafers with a spreading speed of 500 rpm for 20 seconds, and spun at variable spinning speeds for 30 seconds to establish the film thickness.

Once spun, the films were stabilized by heat-treating at 65°C for 5 minutes on an open-air hotplate to drive off the DMF (heating over ~ 70°C results in the DMF breaking down within the film, directly effecting the quality of the films) and oven baked at 150°C for 60 minutes to set the polymer. The Torlon films passed the scotch tape test and adhered well when wafers were diced. This indicates the high adhesion of Torlon to a variety of substrates and its corresponding suitability for use in practical devices. Thicknesses of the films were measured using a Tencor Alpha Step 200 profilometer, the relationship between film thickness and spin speed is shown in Fig. 4.1.1. The spin dynamics of the liquid polymer on all test substrates were sufficiently close that a single spin curve is representative.

Dilute polymer solutions typically exhibit a power law relationship between shear stress and strain rate [39] suggesting a similar relationship for the spin characteristics. Under this assumption a good fit ($R^2 = 0.9775$) was found with the following equation

$$t = 884.34 s^{-0.7242} \simeq 6.1\left(\frac{1000}{s}\right)^{0.72} \qquad (4.1.1)$$

where t is the film thickness in microns, and s is the spin speed in rpm.

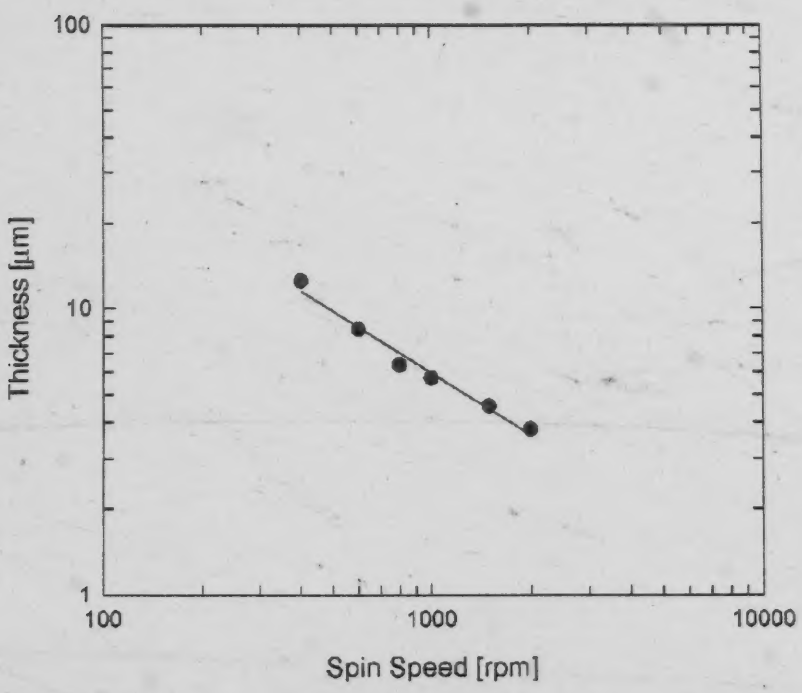

Figure 4.1.1. Spin curve of Torlon on test wafers. Note that the spin characteristics are nominally described by power law behaviour.

Reactive ion etching (RIE) was performed to define features in the Torlon film to test etchability. Figure 4.1.2 shows an alignment mark with an etch depth of 2 µm, with an Au etch mask in place. A more highly magnified view of this feature is shown in the inset. Good verticality is achieved, demonstrating anisotropic etch characteristics. The etched surface of Torlon shows little roughness (3 nm rms, measured on a Digital Instruments Nanoscope III AFM in contact mode) even after etching to a depth of 2 µm; while sidewall striations can be directly attributed to roughness in the Au mask.

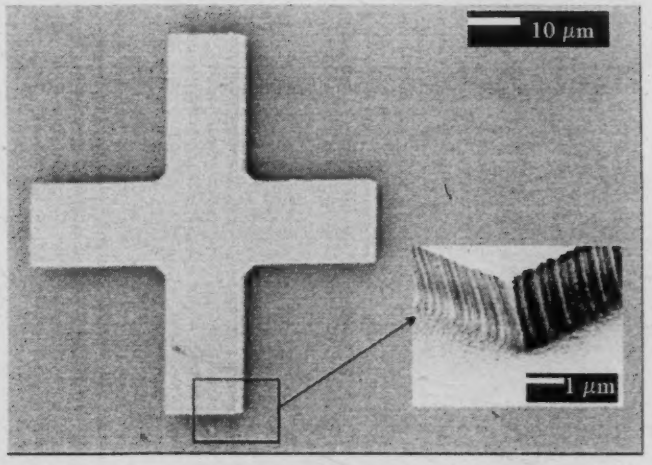

Figure 4.1.2. SEM micrograph of alignment mark eched into Torlon. Inset: magnified detail of etch wall. There is little roughness on the etched surface, though striations from the Au mask can be clearly seen.

Using a Perkin Elmer Lambda 900 Spectrophotometer, the transmission spectrum was found between 700 and 2000 nm. A Cauchy dispersion fit, extracted from the transmission spectra with Swanepoel's method (Appendix 2), is

$$n^2 = \frac{A}{\lambda^2} + B \simeq (1.64)^2 \left[1 + \left(\frac{125}{\lambda} \right)^2 \right], \qquad (4.1.2)$$

where A is 41773 , B is 2.6932, and the wavelength, λ, is in nanometers. Figure 4.1.3 displays the experimentally derived data, and the least squares fit to the Cauchy relation. The least square (50%) error gives a relative error bound on the index of < 0.0025, confirming that a Cauchy fit is appropriate. The absolute accuracy of indices found by Swanepoel's method is on the order of 1% of the calculated value for uniform films (~ 0.02 here). The manufacture's application bulletin for Torlon gives an index value of 1.656 (unspecified wavelength), which is within the range reported here[3].

[3] A refractive index of ~1.64 is large for polymers. Typical values are ~1.5, while Teflon AF (amorphous fluorinated Teflon, PTFE) has the lowest known value of refractive index for polymers, as low as ~1.29 for high glass transition temperature PTFE. Note that the refractive index of water is ~1.33, opening up the possibility of liquid cored photonic devices.

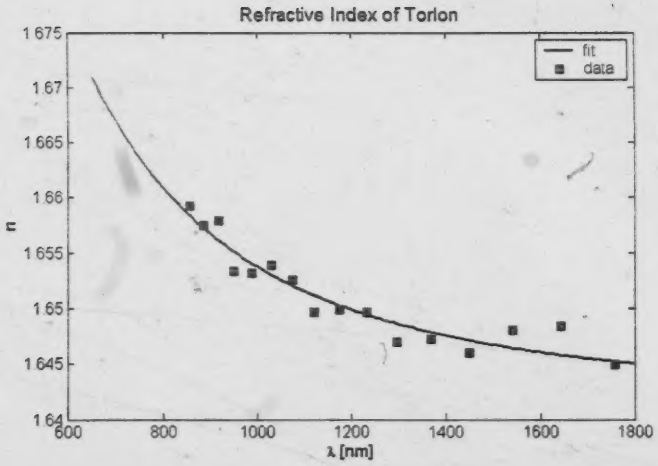

Figure 4.1.3 Torlon index data. Solvay's application bulletin reports an index value of 1.656 for bulk material at an unspecified wavelength, consistent with values measured here for thin films.

Inverted, oversized rib waveguides (Appendix 2) were created with Torlon (core) and BCB (undercladding) as a test case system, Fig. 4.1.4 shows the facet that was end-fire coupled with 830 nm light and the resulting loss streak. Total losses (absorption, scattering) of 0.3 dB/cm were measured, indicating suitability for waveguiding (losses $\leq$ 0.5-0.4 dB/cm are suitable for applications [38], [9]). Inherent absorption losses for optical polymers, such as the related polyimide polymers, are < 0.1 dB/cm [2] and it has been shown for other polymer waveguides [33] that scattering losses can be reduced an order of magnitude below the absorption losses, indicating that improvement can be made in reducing losses. Roughness caused by plasma etching, typically a dominant source of scattering loss, is difficult to completely remove as polymer aggregates of > 30 nm occur in standard (photolithographic) resist polymers [40]. Aggregate sizes can be reduced to ~ 10 nm by using specialized resists, placing a bound on the minimal roughness achievable with standard lithography.

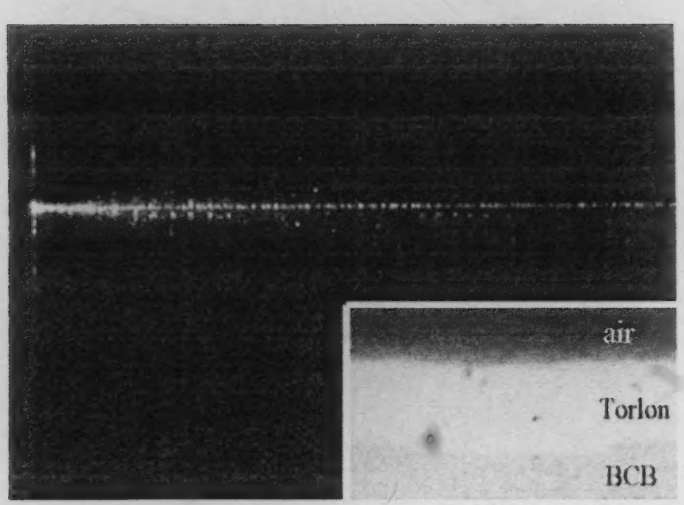

Figure 4.1.4. Loss trace of Torlon Waveguide on BCB undercladding. Inset: End view of an inverted rib waveguide, with Torlon core layer and BCB undercladding. The presence of speckles in the film indicates particulate scattering centers.

4.2 Laser Ablation of Polymers for Grating Fabrication[4]

Gratings can be located in either the cladding material, or the core material. Laser ablation can be used to directly write gratings in polymer materials, potentially allowing rapid, low-cost, grating fabrication.

Direct production of gratings has been studied for standard "ablation polymers" such as polyimide [41], [42], as well as in specialty polymers designed for ablation [43]. In the present work, ablation for the direct production of gratings on spun cast films (Torlon, BCB, PET) and commercial PET (Mylar) sheets was investigated.

A narrow bandwidth krypton fluoride (KrF) laser producing 25 ns pulses at an output wavelength of 248 nm was used, similar to the laser in [41]. A Mach Zehnder setup was chosen (Fig. 4.2.1) where the two beams are brought together on the polymer film at

[4] A version of this chapter has been published. R. M. Bryce, R. G. DeCorby, J. N. McMullin, and Y. Y. Tsui, "Direct Production of Gratings on Polymers using UV Laser Radiation", Proceedings of the International Conference on MEMS, NANO and Smart Systems, 172-176, 2003.

approximately equal angles of incidence θ, and a movable 1 m focal length lens allowed intensity to be varied.

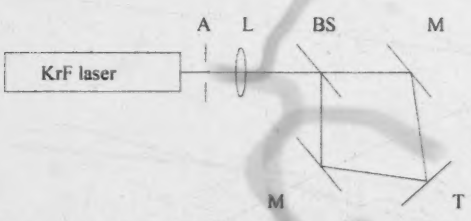

Figure 4.2.1 Experimental Setup. A laser pulse from the KrF laser passes through a 1cmX1cm aperture (A), focuses through a lens (L), is split into two with a beam splitter (BS), and brought back together with two mirrors (M) onto a target (T) film. The linewidth is 0.1 cm^{-1} and windows are set to the Brewster angle. Approximately 10 mJ of energy was available after the aperture in the setup used.

Intensity maxima and minima results from interference causing energy to be deposited in a periodic structure with a period Λ given by

$$\Lambda = \frac{\lambda}{2\sin\theta} \qquad (4.2.1)$$

As polymers typically have thermal diffusivities D of $\approx 10^{-3}$ cm^2/s [44], diffusion lengths of the order $\sqrt{D\tau} = 50$ nm are expected. This indicates that energy will be confined within the λ/2 minimal interference bands obtainable. As energy is localized within band structures, nonuniform ablation results in direct production of gratings. Polymer films used were thicker than 0.5 μm, well above the thermal diffusion length. For polymers to be suitable for ablation, short optical absorption depths ($\sim\alpha^{-1}$, where α is the absorption coefficient) are required to localize optical energy in small volumes, and "good" ablation is required. Good ablation is an empirical quantity, qualified by sharp features and a lack of burning, melt flow, or backsplash (redeposition of material)[5].

[5] It is observed that the inclusion of ring structures (such as benzene like groups) on the polymer backbone and a close by weak bond (often nitrogen link) leads to strong absorption and clean ablation. The ring structure likely acts as an antenna to absorb incident radiation, while the close by weak link allows polymer damage without thermalization effects.

Threshold fluences for the onset of ablation were found by visually identifying the onset of surface damage. It was observed that ablation had a sharp onset, with an ablation plume ("smoke") occurring when surface damage was observed. In the BCB and Torlon polymers a single, sharp, transition was observed; in the Mylar polymer a sharp transition was found, in addition to a weaker effect where surface modification tapered off as incident energy was decreased. The energy of the laser pulses was measured by a pyroelectric calorimeter and the laser beam area was deduced from the damage area at the laser irradiated polymer surface. Error in measured fluences are estimated at 25%, due to calorimeter error and error in measuring the damage area.

The threshold fluences for the polymers were found (see Table 4.2.1). The weaker surface modification of Mylar tapered off around 6 mJ/cm^2. Sheet Mylar polymer is well studied, and has a reported fluence of 30 mJ/cm^2 [45], agreeing with our value within error. Sheet Mylar polymer is a quasi-crystalline material, and has a calculated amorphization threshold of 3.6 mJ/cm^2 for 25 ns 248 nm pulses [46]. Over this threshold the rapid heating and cooling of the polymer subsurface results in a phase change. The agreement of our values with reported values for Mylar increases confidence in the suitability of visual identification of thresholds.

Table 4.2.1 Polymer Ablation Thresholds.

Polymer	**Threshold** (mJ/cm^2) error ~ 25 %
Benzocyclobutene (BCB)	80 +/- 20
Torlon (PAI)	26 +/- 6
Mylar (PET)	35 +/- 9

All grating samples showed eventual deterioration when multiple shots were used to form gratings. In Mylar the surface obtained a milky hue, while in BCB and Torlon a sooty material formed on the surface, indicating that single shot formation of gratings is preferable.

AFM images were taken of Mylar gratings in contact mode (Fig. 4.2.2, 4.2.3), which demonstrate that strong gratings are achievable with ~ 1 μm periods.

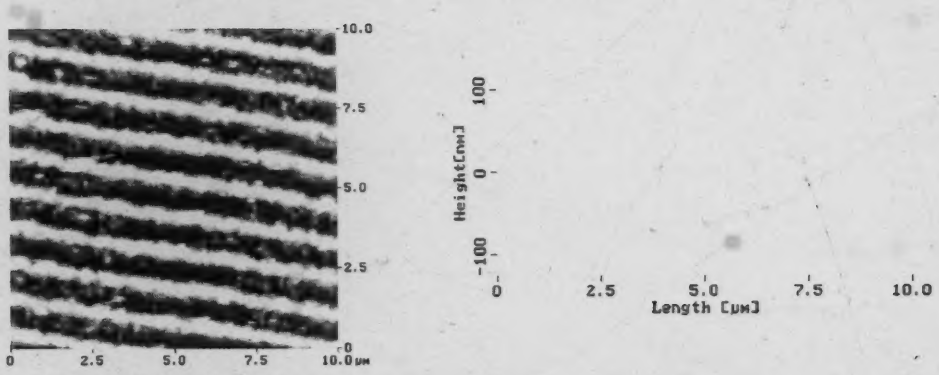

Figure 4.2.2 AFM micrograph of ablated grating in Mylar film. Here multiple shots were made and the deterioration of the polymer can be seen. The structure is deeper than single shot gratings, and shows signs of deterioration.

SEM analysis of Mylar gratings demonstrates that uniform grating structures are achievable (Fig. 4.2.3, left image), and that 175 nm period gratings, which approach the theoretical minimum of the setup (124 nm; see Fig. 4.2.3, right image), are possible.

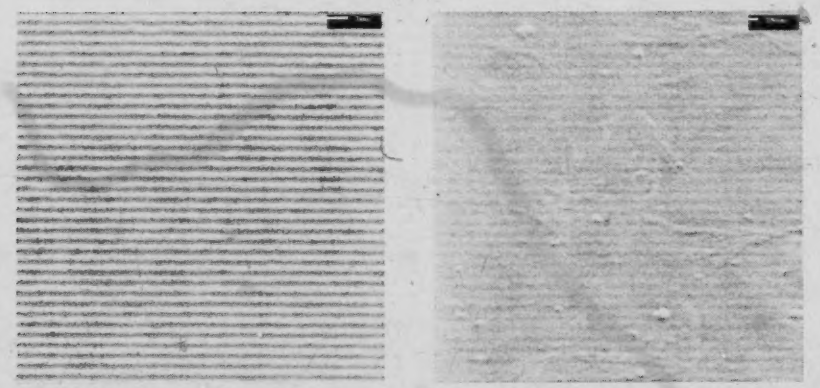

Figure 4.2.3 SEM Micrograph of ablated Mylar grating. Scale bar for the left hand image is 1 µm, and 100 nm for the right hand image. In the right hand image the feather like features are part of the Mylar sheet film, while the spots appear to be molten plastic backsplattered onto the surface. Reducing the period results in reduced grating depth (strength).

Shallower gratings were achieved in BCB and Torlon films, and surfaces had high amount of debris (Fig. 4.2.4, 4.2.5). This debris was loosely bound, washing off with an IPA rinse/air gun dry cycle.

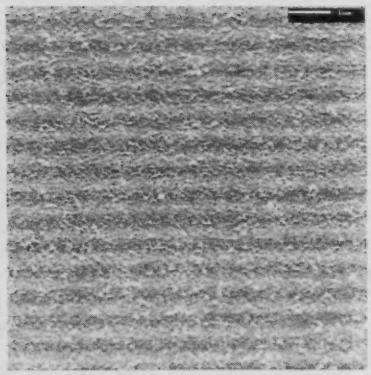

Figure 4.2.4 SEM Micrograph of ablated BCB Grating. Scale bar 1 μm. Shallow gratings of ~ 800 nm period can be clearly seen.

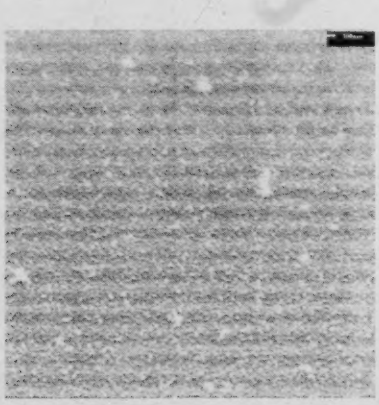

Figure 4.2.5 SEM Micrograph of ablated Torlon grating. Scale bar 100 nm. Debris is loosely bound; cleaning samples with alcohol washes the debris away.

As Mylar gratings had the highest quality, the feasibility of spun-cast Mylar films was investigated. Mylar sheets were dissolved in o-chlorophenol solvant [47] and spun-cast on SiO_2 wafers. Mylar is very inert and resistant to chemical attack, and phenol based solvents only mildly dissolve Mylar. A target ratio of 1 g of Mylar per 10 mL of o-chlorophenol was set, but could not be achieved – most of the Mylar remained

undissolved, even after several weeks[6]. This solution was filtered and spun at 300 rpm. A soft bake of 50 °C for 15 min was followed by a bake at 140 °C for 1 hr. Films of ~ 1 μm thickness were obtained.

AFM analysis of film surfaces indicates that modification from a polycrystalline phase occurs (Fig. 4.2.6) [46]; suggesting the crystals are formed due to fabrication from melt. The surface roughness of the spun cast films is ~ 10 nm, which is twice that measured on Mylar sheets (~ 5 nm). The lack of embedded crystals in spun cast Mylar is desirable, as these crystals will increase scattering losses.

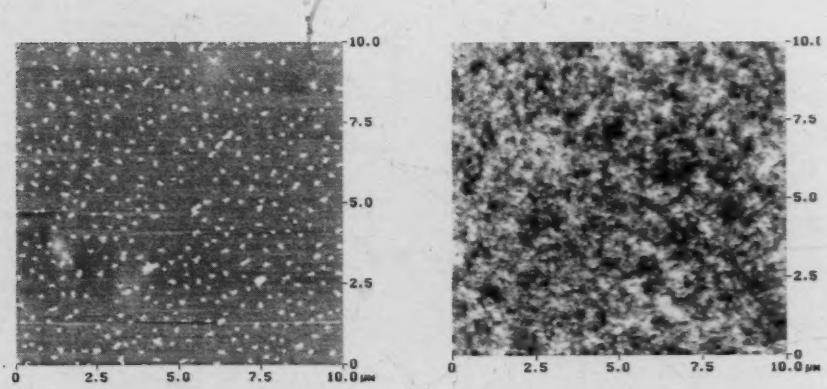

Figure 4.2.6. AFM micrographs of Mylar films. Sheet Mylar (left hand image) has ~ 20 nm crystals embedded within the film. Note the lack of crystals in spun cast Mylar (right hand image).

Gratings formed on spun cast Mylar (Fig. 4.2.7) with quality in between BCB/Torlon and sheet Mylar. The underlying surface structure is not smooth, indicating that refinement of spun cast film processing is required.

[6] Other solvents are being sought, as well as investigating the use of elevated temperature dissolving. A general rule of thumb is that the reaction rate will double with every 10 °C raise in temperature. Currently work with o-chlorophenol has proven the most promising, and solutions with ~1g/10mL have been obtained. The solution is very viscous, and filtering is difficult (vacuum assisted filtering is required).

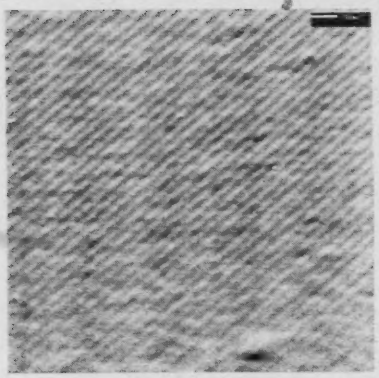

Figure 4.2.7. SEM Micrograph of ablated gratings on spun cast Mylar. Scale bar 1 μm. Note the lack of back splatter, versus Mylar sheets.

It has been found that BCB/Torlon can be used to fabricate single shot ablated gratings, and that spun cast Mylar is a promising material. Unfortunely laser beam quality in the system used is insufficient to produce large area (~mm to cm sized) gratings of high quality and uniformity, and spatial filtering or improved optics would be required to allow large area grating formation. For waveguiding applications grating structure has a strong effect on optical response, making strict control of structures critical.

4.3 Slab Waveguiding in Chalcogenide Films

Commercially obtained arsenic triselenide (As_2Se_3, Alfa Aesar) was deposited with thermal evaporation; with a deposition rate of approximately 2 nm/s. Films of approximately 3 μm thickness were formed on undercladdings (held on standard 4" Si wafer substrates). The wafers were positioned 12" from the sample boat, rotated during deposition, and kept under a vacuum of $2*10^{-6}$ Torr.

Torlon and BCB undercladding were investigated, as polymers adhere well with a majority of materials and their thermal expansion coefficients are more matched to chalcogenide glasses than most other optical materials. Oxide coated Si was also investigated, as this is a standard material. Both oxide and Torlon undercladding worked well; it was difficult to obtain cleaves with BCB that would not need polishing. Due to an

intermittent supply of oxide coated wafers work focused mainly on Torlon undercladdings.

The Scotch tape test[7] was performed to verify good adherence of the film on the substrates, and dicing of the wafer with a diamond tip pencil was performed. Difficulty in finding a suitable process and undercladding for the arsenic triselenide was experienced, with the majority of attempted trials resulting in films that shattered upon dicing. Figures 4.3.1 and 4.3.2 demonstrate that a sharp dices were eventually achieved with Torlon undercladding, allowing coupling of light without the need for polishing (see Fig. 4.3.3). Sharp dice interfaces were achieved when experience was gained in exerting proper pressure. It should be noted that when Torlon undercladdings exceeded 6 μm in thickness the films tended to peel off of the Si substrate on cleaving.

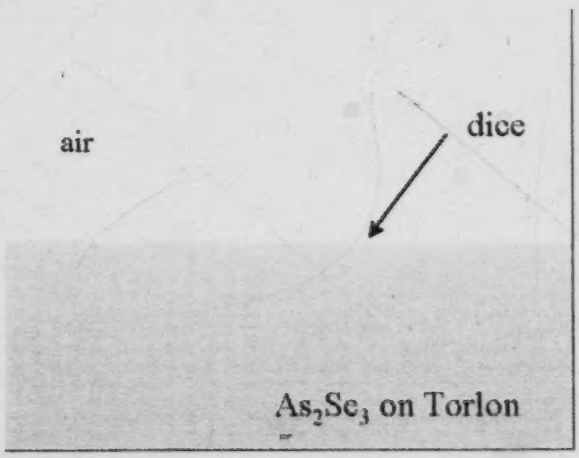

Figure 4.3.1: Top view of diced slab structure on Si wafer at 100X magnification. A sharp interface was obtained.

[7] The Scotch tape test is a pass/fail test ensuring a minimum threshold adhesion is surpassed. This test is commonly used, giving a practical measure of "hardy" films. The test is related to the U.S. military standard specification MIL-STD-883C.

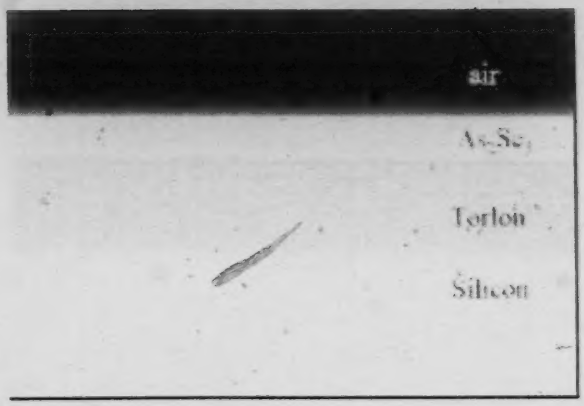

Figure 4.3.2: End facet of slab waveguide system, under 100X magnification. A distinct and smooth facet was obtained after cleaving and the chalcogenide layer was undamaged over most of the cut, with the exception of locations were the Si wafer exhibited mechanical damage. The Torlon layer is ~ 6 μm thick.

It is likely that shattering arises from two factors. Stresses are trapped in the chalcogenide layer during cooling after deposition, induced by mismatch in thermal expansion coefficients involved (mismatch of ~5 ppm/°C for Torlon, and ~ 20 ppm/°C for oxide), and can lead to rupture of films. Chalcogenide glasses typically have thermal expansion coefficients an order of magnitude larger than most important substrates, making this a dominant concern [9]. In addition dicing was done by hand, and often the underlying Si wafer itself was not cleanly cut – indicating human-induced damage may play a strong role. The construction of an automated dicing instrument could increase the quality of cuts, and as heavy damage in the wafer potentially acts as a center for failure of chalcogenide films, strong improvements in facet quality could be gained.

Arsenic triselenide is transparent in the range of ~0.8 to 17 μm [48], allowing 830 nm light to be used to test waveguiding. This wavelength was selected, as Si detector CCD cameras were available for imaging. Fibre coupling was performed on a coupling station that allowed an optical fibre to be brought into contact with the slab waveguide. Strong coupling was achieved along the entire diced facet, and loss streaks photographically obtained qualitatively indicate that low loss waveguiding is exhibited in the

Chalcogenide/Torlon system[8]. In particular a lack of bright "speckles" in the excited film (compare with Fig. 4.1.4) demonstrate a lack of impurities and scattering centres, and the slow drop off in streak intensity demonstrates good confinement.

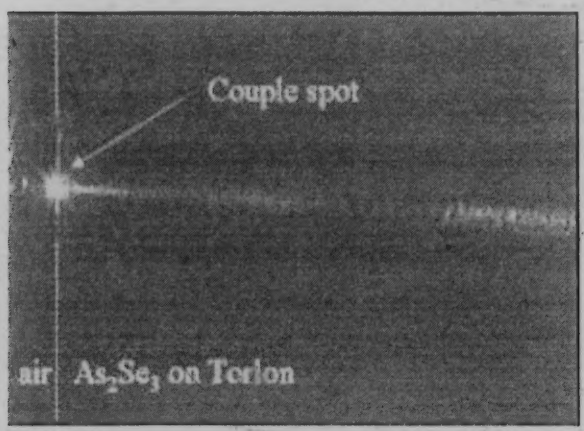

Figure 4.3.3: Coupling 830 nm light into slab waveguide. The loss streak can be seen propagating along the slab. Notice the absence of speckles in the film, indicating a corresponding absence of imperfection and scattering centers.

The successful formation of a slab waveguide structure, and achievement of coupling, demonstrates the suitability of the chosen material set for use in integrated optical devices. The ability to obtain smooth facets is a highly desirable property, as polishing of surfaces is typically required for coupling. By removing the need to polish, health concerns are minimized, while time consuming and potential mechanically damaging steps are avoided.

4.4 Inverted Rib Structures

Design initially centered on inverted rib waveguides, due to the ability to create oversized guides that reduce fabrication and coupling difficulties. The inverted structure was chosen, as chalcogenide glasses can be etched only to limited depth by either plasma or

[8] Scattered light (Fig. 4.3.3) indicates ~2-3 dB/cm loss occurs. This number is, at best, a rough estimate as light will laterally spread out, and back-reflection at the end of the slab interferes with data fitting.

chemical etching [49]. For example, when chemical etch depths surpass ~ 0.1 μm underlying films start to dramatically fail (often cracking, or peeling away from the substrate), imposing a limit on achievable structures. Wicking of solvent at the chalcogenide glass/undercladding interface likely induces this failure.

Inverse rib waveguides allow the poor etching quality of chalcogenide to be avoided. Patterns are defined in a substrate, and chalcogenide is deposited on top. The process available for deposition was thermal evaporation. Evaporated glass condenses on substrates, faithfully transferring substrate features resulting in very smooth films, characterized by nanometer-sized roughness. This was also found to result in etched patterns transferring through the film, which negatively affects devices, as planarization of the top layer is required for proper performance of waveguides.

Plasma etching of waveguide trenches in the underlying polymer layer was done. Deep reactive ion etching (Deep RIE) directs plasma unto the surface resulting in a unidirectional etch (see Fig. 4.1.2). Equipment problems at the microfab required the use of an undirected plasma etcher, which results in structures having a reduced aspect ratio and rougher surfaces (with deteriorating quality as etch depth is increased). Figure 4.4.1 and 4.4.2 illustrate the structures obtained in BCB and Torlon polymers.

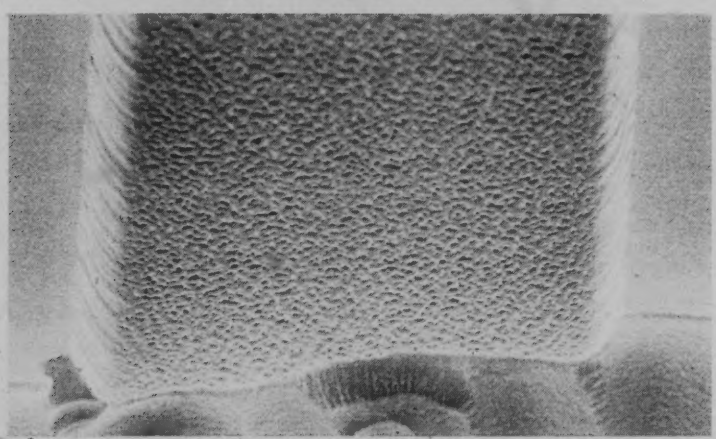

Figure 4.4.1 Plasma Etch of Torlon. Nominally 10 μm wide and 1 μm deep trench test structure for inverted rib waveguides.

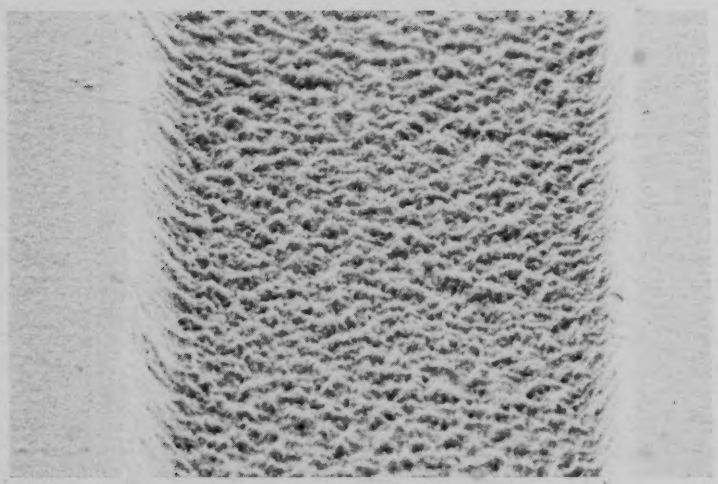

Figure 4.4.2 Plasma Etch of BCB. 4 μm wide and 0.5 μm deep trench test structure for inverted rib waveguides.

Oxide undercladdings were also used, with wet etching used to create waveguides. Plasma etching of oxide results in porous surfaces plagued by pillar structures (see Fig. 4.4.3); deposition of chalcogenide on these surfaces creates a porous waveguide channel. Chemical etching of plasma-etched oxide cleans away pillars (Fig. 4.4.3, inset), but as this method was time-intensive, efforts were focused on plasma etched polymer and chemically etched oxide undercladdings.

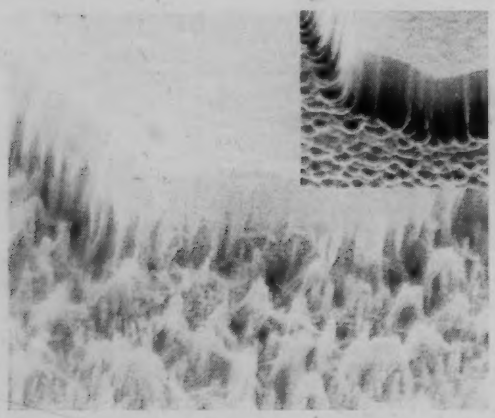

Figure 4.4.3 Plasma etch of oxide. Inset shows post treatment by chemical etch to remove pillars. The "bevel" corner is ~ 1.5 μm long. Substantial roughness remains even after chemical treatment.

Chalcogenide glass was deposited on etched structures defined in oxide and Torlon. While both low and high spatial frequency imperfections on the surface were directly transferred during deposition (see Fig. 4.4.4 and Fig. 4.4.5) the bulk did not exhibit pillar structuring. At the edges of the waveguides the film often experienced a physical gap. As the trench depth was increased the imperfections increased, as expected.

Figure 4.4.4 Chalcogenide glass deposited on Torlon. A 4 μm wide and 0.5 μm deep trench was plasma etched into Torlon. 10 μm of chalcogenide was evaporated on top. Surface roughness in the trench is transferred thoughtout the glass, but within the film no pillar structure exists.

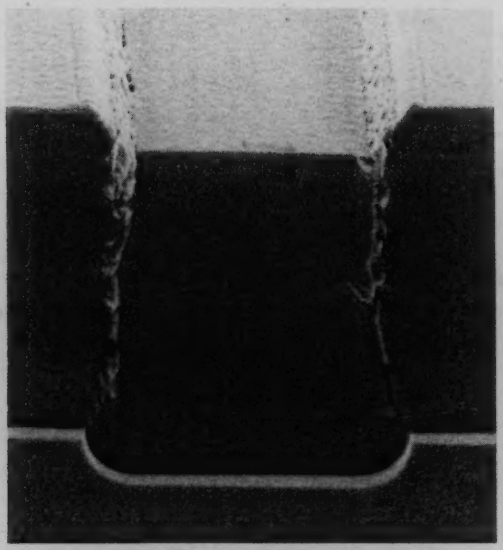

Figure 4.4.5 Chalcogenide glass deposited on oxide. A 4 μm wide and 0.5 μm deep trench was chemically etched and chalcogenide was evaporated on top. Note the mismatch between the undercladding and chalcogenide film, visibly demonstrating expansion effects.

Annealing was attempted to smooth the physical gap observed at the edge of the waveguide structures, to remove possible bulk inhomogeneities, and to reduce the dip on the surface of the film, by causing material flow. Diced sections of 2-3 cm length and full wafer width were heated to 140°C for 2 hours in a vacuum oven. Full wafer films often experienced cracking, due to release of heat expansion induced stress.

The Torlon undercladding samples appeared to buckle in some spots, possibly due to out-gassing or stress relief; but no cracks were observed visibly or under microscope and SEM analysis. Oxide undercladding samples appeared free of surface damage, but SEM micrographs indicate waveguide structures acted as stress release points, occasionally resulting in cracking within the waveguide section (Fig. 4.4.6). Inspection of SEM micrographs showed no observable improvement after annealing, and no signs of material flow.

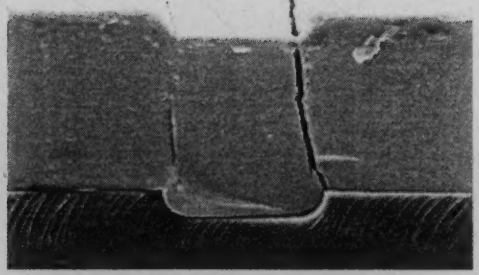

Figure 4.4.6 Annealing induced fracture of chalcogenide. Oxide underclad samples experienced cracking within waveguide sections due to stress release. The thermal expansion mismatch between oxide and chalcogenide causes stress during heating and cooling, the waveguides are weak regions that act as breakage points.

Evaporated films rely on a process that condenses material from a gas phase directly to a solid phase – the lack of a fluid intermediate stage results in an inability for deposited material to flow. This immediate freezing of material will faithfully reproduce the underlying structural profile, and planarization does not occur. In general, it is well known that sputtering of films is more complex than evaporation, but is a superior deposition technique. This rule of thumb has been found to be true for chalcogenide glasses [50], [9], although planarization is not achievable with this technique[9].

Spin casting of As_2S_3 has been reported [51] [52], and this fluid phase deposition technique was attempted. A solution of 2 g of As_2Se_3 was dissolved in 10 mL of amine (ethylendiamine) solvent and spun cast on SiO_2 wafers with waveguide trenches. The resulting films were baked at 100°C in a vacuum oven to prevent reaction with water and oxygen in air. Films deteriorated with growing oxidized spots occurring on the surface. Modification of the oven to allow baking in an N_2 atmosphere was made and care was

[9] Planarization requires a liquid phase to allow flat films to be made, and high intensity lasers are often used to melt and planarize deposited films. Deposition of sacrificial layers and etch back is also commonly used for planarization.

taken to remove the presence of water from the solvent; films were baked in N_2 below atmospheric pressure, resulting in improved quality films (no longer deteriorating) although high quality films were not achieved (dust on the substrate caused streaking). Work on improving films fabricated in this manner was discontinued, as the resulting films were thin (<1 μm); even at low spin speeds.

Due to the difficulties encountered the inverted rib structure was abandoned. It is notable that liquid phase deposition has promise, as it was found that inverted structures could be filled. Evaporation of a film over filled inverted structure is therefore a possible means to fabricate physically patterned chalcogenide layers.

4.5 Photodoped and Photodarkened Structures[10]

The ability to photomodify chalcogenide glasses is one of their most interesting properties, allowing waveguiding structures to be defined by illumination with near bandgap light.

Silver doping was attempted using a mask aligner, as ultraviolet laser mediated silver doping has resulted in high index offsets [53]. Nominally 30 nm thick Ag films were deposited on ~ 2 μm thick chalcogenide glass. After exposure to ultraviolet light on a mask aligner for 10 s and etch of the remaining silver (nitric acid wash) the index of refraction was measured with Swanepoel's method and an index increase of ~0.2 was found. This high index offset is desirable for many device architectures, but was not pursued as part of this work as index offsets two orders of magnitude lower were assumed during mask design.

To test photodarkened structures ~ 3 μm thick chalcogenide film was exposed through a mask with an unfiltered white light (tungsten) source to create waveguide structures. As photodarkening is dependent on exposure level the time of illumination was set to target

[10] A version of this section has been submitted for publication. R. M. Bryce, H. Nguyen, P. Nakeeran, R. G. DeCorby, P. K. Dwivedi, C. J. Haugen, J. N. McMullin, and S. O. Kasap, "Direct UV patterning of waveguide devices in As_2Se_3 films", Proceeding of the Canadian Semiconductor Technology Conference, 2003, Journal of Vacuum Science and Technology A.

an index change of 0.05, though no direct measurement was made to confirm this value. Figure 4.5.1 shows coupling of 830 nm light imaged with a CCD camera and Figure 4.5.2 shows 1550 nm coupling obtained using an infrared InGaAs camera (Model 8128, ElectroPhysics).

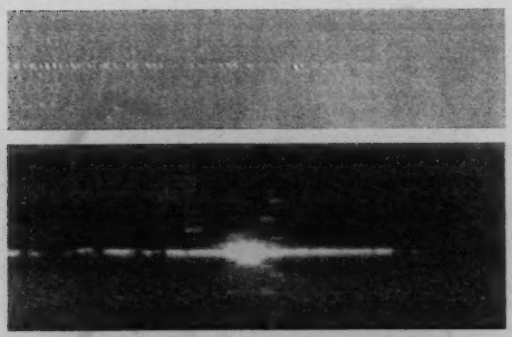

Fig. 4.5.1: Photodarkened Waveguide. A broadband illumination source (tungsten lamp) was used to photodarken chalcogenide glass through a mask. The upper image is a top view of 830 nm light being coupled into the waveguiding structure and the lower image is of the waveguide output.

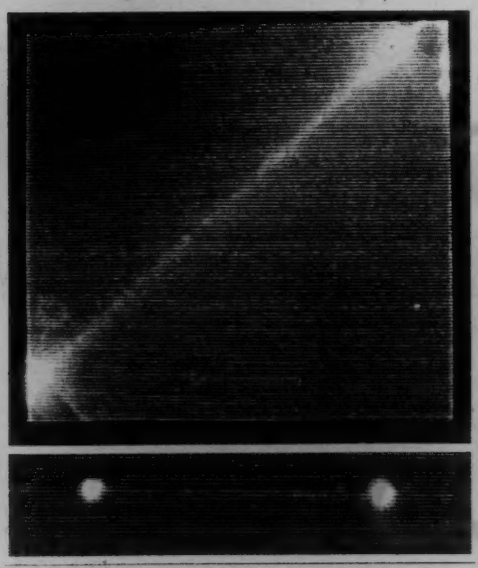

Fig. 4.5.2: Photodarkened Directional Coupler. The upper image is a top view of 1550 nm light being coupled into the waveguiding structure defined with broadband illumination (tungsten lamp); the light is coupled in the upper right corner and propagates to the lower left. The diced edges can be observed in the corners of the upper image. The lower image is of the end view (output) of the directional coupler, note the faint illumination line corresponding to the chalcogenide film and the bright spots corresponding to waveguides (250 μm separation).

The successful white light photodarkening demonstrates that suitable structures can be obtained with this fabrication method. As chalcogenides experience photodarkening over a broad energy range centered at the bandgap, direct ultraviolet photodarkening using a mask aligner was investigated, as this is a standard tool with well-defined characteristics.

Initial tests of ultraviolet exposure on a mask aligner (17 mW/cm^2 in the 365 nm line, 41.3 mW/cm^2 in the 400nm line; < 2 % error on these values) for 500 s resulted in an increase of ~ 0.04 in index; which is within the index offset range designed for. Currently, a detailed investigation of ultraviolet exposure effects (index modification versus dosage) is being undertaken.

Photodarkened devices are difficult to work with because devices are not clearly visible (making coupling into waveguides difficult, and alignment of subsequent processes problematic). As the dissolution rate of chalcogenides in solvents is reduced by photodarkening [54], this allows a means to physically define photodarkened waveguides. By washing ethylenediamine over photodarkened structures in chalcogenide thin films the differential etch rate (~1.5-2 [54]) will physically define the structures allowing visible identification.

Chalcogenide glass films of 2.5 μm thickness were deposited on borofloat glass and exposed for 500 s under ultraviolet light, with the designed mask in contact mode. The large alignment structures were clearly visible with the naked eye after exposure, and waveguides could be discerned[11]. The exposed film was etched for one minute in ethylenediamine heated to ~ 50°C, quickly rinsed with deionized water, and dried with an air gun. Initial chalcogenide films were nonuniform with pinholes and imperfections, leading to film failure and peel away in spots, but overall good etch characteristics were obtained. Waveguides were clearly visible with naked eye, and an etch depth of ~ 0.1-0.2 μm was measured with a profilometer. Using Torlon undercladding improved etch quality, no peeling occurred. Features transferred accurately from the mask to the

[11] Borofloat is transparent, allowing transmission rather than reflection observation of photodarkened structures.

chalcogenide glass in the mask aligner, with 4.05 +/- 0.02 μm features arising from 4 μm sized features on the mask. Locally etch quality was superior to that obtained with polymer photoresist, where difficulty was experienced in getting uniform etch characteristics over directional coupler regions. Figure 4.5.3 demonstrates the etched features obtained.

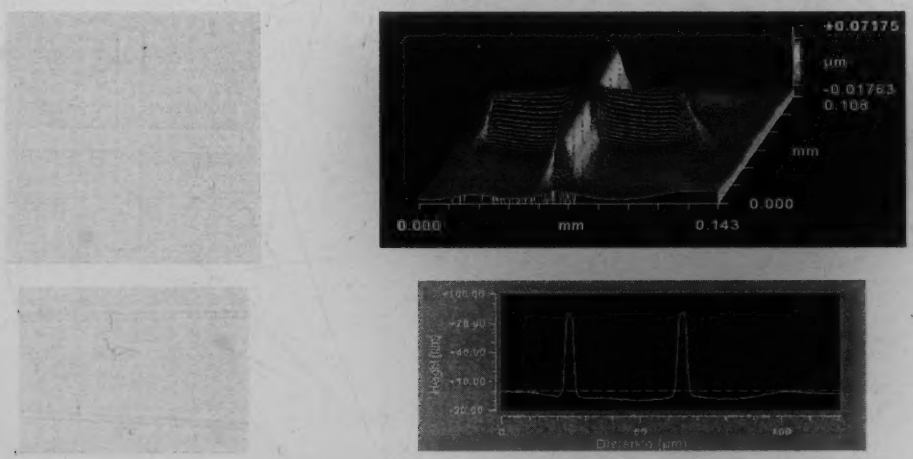

Fig. 4.5.3 Photodarkened and etched test features. Alignment mark (top) and directional coupler regions (bottom) are defined by photodarkening followed by a chemical etch. Optical microscope images (left) demonstrate the clear features obtained, while optical spectrophotometery (right) shows high etch contrast is obtained.

A concern in ultraviolet exposure is achieving sufficient penetration into chalcogenide films, as well as uniformity over the depth, due to high absorption coefficients typically exhibited for ultraviolet light by materials including chalcogenides [55]. While absorption lengths of ~ 0.1 μm are expected for ~ 200 nm ultraviolet light versus ~ 1 μm absorption depths for ~ 600 nm light [55] it is noted that mercury bulbs have their peak emission line at 400 nm, resulting in an absorption length between these levels. Experiments on As_2S_3 glass on 0.4-0.8 μm thick films exposed with quartz filtered Hg vapor lamp light [56] indicate that penetration and uniformity is achieved to a sufficient level for films on the sub-micron scale to allow envelope based transmission spectrum determination of index and loss. It should be stressed that "absorption lengths" are a characteristic length scale used to impose a convenient metric, here the scale bar is set to the length where 1/e of the energy is absorbed, meaning that ~ 2/3 of the energy will be

absorbed within this length. This leaves ~1/3 of the initial energy available to be absorbed within the next absorption length, explaining the possibility of photodarkening at depths below the absorption length. It is known that the amount of refractive index modification due to photodarkening saturates in chalcogenide glass. This may allow indefinite penetration given long enough exposure times, if absorption bleaching is associated with this saturation.

As the initial inverted rib structure has been abandoned, thinner films can be used and films below 2 μm constitute a target for photodarkened structures. This thickness is a trade off between the singlemode requirement and the absorption length, which require thin structures, against the desire to simplify fibre coupling, which is facilitated by thicker films.

5. Summary and Recommendations

5.1 Overview of Significant Results

The goal of this work was the construction of an optical add-drop filter in chalcogenide glass. While a working device was not achieved in the end, a number of achievements were made, several of which bring this goal closer to realization:

- simplified rules were found for oversized rib waveguides;
- a method to correct the difference between directional coupler spacing as designed, and obtainable with processes used in fabrication, was found. This correction is made by modifying the film thickness from the designed case;
- a simple method to guide the tapering of directional couplers was discovered;
- sulfone thin films were fabricated;
- Mylar (PET) thin films were fabricated;
- Torlon (PAI) thin films were fabricated, and demonstrated to be useful for integrated optics;
- gratings were ablated in Torlon, BCB, and Mylar polymers;
- slab waveguides were made in chalcogenide glass;
- channel waveguides were formed in chalcogenide glass by photodarkening;
- silver photodoping, using a mask aligner, was shown to substantially increase the refractive index;
- it was show mask aligners could be used to form photodarkened waveguides; and
- post-treatment of photodarkened regions with chemical enchants was show to create physically defined waveguides.

Work on Mylar and sulfone films, as well as ultraviolet photodarkening, continues.

5.2 Suggestions for Future Work

Investigation of sputtering for the deposition of chalcogenide is a promising avenue, as it allows for deposition of films with various compositions (as evaporation rates, which are highly material dependent, are not the mechanism used for deposition). As sputtering is used in industry, whereas evaporation mainly remains a "laboratory" process [22], results obtained within this framework are also more likely to make an impact in industry. Sputtering is performed with plasma bombardment, so that plasma etching of chalcogenides can take place with the sputter device [49]. We currently do not have the capability to sputter films, as the toxicity of As_2Se_3 prevents use in general-user sputter devices; the broader applicability of sputtering, versus evaporation, makes attaining this capability desirable.

The close proximity of waveguides in directional couplers leads to difficulties in fabrication (due to resist induced roughness [40], contamination, dependence of etch rates on geometry, etc). These difficulties make modification to zero separation directional couplers (low mode number multimode interference (MMI) devices) a reasonable step. The Bragg-grating assisted MMI-coupler arrangement has been recently proposed and investigated [57].

Arsenic triselenide is toxic, and the investigation of reduced toxicity chalcogenide glasses is underway. Deposition of Ga-La-S chalcogenide films are being investigated at TRLabs using pulsed laser deposition, in collaboration with Y. Y. Tsui (Laser-Plasma Interactions group, University of Alberta). Ga-Ge-Se based glasses offers some possible advantages, such as reduced toxicity, and investigation of these glasses is suggested. In the case of As-Se and As-S systems the Se based glasses demonstrate stronger photodarkening, without an associated photoexpansion, versus the S based glasses (expansion has also been observed in Ga-Ge-S glasses [58] [59], indicating the role of S in this effect). Ga-Ge-Se glasses can be thermally deposited, and films made with these glasses been widely studied. There appears to be few studies of photo-induced modification of refractive

index in Ga-Ge-Se, though the presence of these effects in Ga-Ge-S glasses [58], [59] and work on Ge-Se [60] and Ge-Se-Te glasses [4] indicates that these effects exist. Further, As-based glasses tend to have poor doping capability versus Ga-Ge-Se glasses.

It is notable that ultraviolet exposed and etched chalcogenide glass appears to have superior characteristics than traditional polymer resist lithography, which will allow for improved fabrication. The spun-cast chalcogenide films investigated here could not be made thick enough for optical waveguiding, but may offer a simple means to improve lithography. Chalcogenides have been investigated for lithography applications [55]. Investigation of spun-cast and evaporation deposited films, of reduced toxicity chalcogenides, for lithography may be warranted.

The small structures required for integrated optics makes coupling to optical fibres a challenge, and the investigation of structures to improve coupling would be quite useful. For example width-tapered waveguides; grating structures to allow butt coupling of fibres, to the top surface of waveguides; microlenses, and other structures could be used.

As work progresses towards working devices, accurate control over deposited film thickness will become critical. Accuracy achieved, with the current setup, is on the order of a micron. This accuracy is insufficient to allow fabrication of as-designed structures, and must improve by several orders of magnitude.

References

[1] S. E. Miller, "Integrated optics: An introduction", Bell Systems Technical Journal, 48 (7), 2059-2069, 1969.

[2] L. Eldada, "Advances in telecom and datacom optical components", Optical Engineering, 40 (7), 1165-1178, 2001.

[3] Y. Utsugi, and Y. Mizumima, "Lattice-dynamical aspects in photoexcited chalcogenide glasses", Japanese Journal of Applied Physics, 31(12A), 3922-3933, 1992.

[4] A. F. Maged, A. M. Sanad, M. F. El-Fouly, and G. A. M. Amin, "A study of optical absorption and photoinduced effects in Ge-Se-Te amorphous system", Journal of Material Science, 13(5), 1128-1131, 1998.

[5] K. Tanaka, "Photoinduced processes in chalcogenide glasses", Current Opinion in Solid State and Materials Science, 1(4), 567-571, 1996.

[6] G. Lenz, J. Zimmermann, T. Katsufuji, M. E. Lines, H. Y. Hwang, S. Spälter, R. E. Slusher, and S.-W. Cheong, "Large Kerr effect in bulk Se-based chalcogenide glasses", Optics Letters, 25 (4), 254-256, 2000.

[7] A. C. van Popta, R. G. DeCorby, C. J. Haugen, T. Robinson, and J. N. McMullin, "Photoinduced refractive index change in As2Se3 by 633nm illumination", Optics Express, 10(15), 639-644, 2002.

[8] T. G. Robinson, R. G. DeCorby, J. N. McMullin, C. J. Haugen, S. O. Kasap, and D. Tonchev, "Strong Bragg gratings photoinduced by 633-nm illumination in evaporated As_2Se_3 thin films", Optics Letters, 28(6), 459-461, 2003.

[9] S. Ramachandran, and S. G. Bishop, "Low loss photoinduced waveguides in rapid thermally annealed films of chalcogenide glasses", Applied Physics Letters, 74(1), 13-15, 1999.

[10] P. N. Kumta, and S. H. Risbud, "Rare-earth chalcogenides – an emerging class of optical materials", Journal of Materials Science, 29(5), 1135-1158, 1994.

[11] F. Bakhti, P. Sansonetti, C. Sinet, L. Gasca, L. Martineau, S. Lacroix, X. Daxhelet, and F. Gonthier, "Optical add/drop multiplexer based on UV-written Bragg grating in a fused 100% coupler", Electronic Letters, 33 (9), 803-804, 1997.

[12] D. J. Griffiths, Introduction to Electrodynamics, 3rd Ed., Prentice Hall, 1998.

[13] A. R. Mickelson, Physical Optics, Van Nostrand Reinhold, New York, 1992.

[14] A. Yariv, Optical Electronics in Modern Communications, 5th Ed., Oxford University Press, New York, 1997.

[15] P. Yeh, Optical Waves in Layered Media, John Wiley & Sons, New York, 1988.

[16] M. A. Muriel, A. Carballar, and J. Azaña, "Field Distributions Inside Fiber Gratings", IEEE Journal of Quantum Electronics, 35 (4), 548-557, 1999.

[17] K. S. Chiang, "Performance of the effective-index method of the analysis of dielectric waveguides", Optics Letters, 16(10), 714-716,1991.

[18] A. Kumar, D. F. Clark, and B. Culshaw, "Explanation of errors inherent in the effective-index method for analyzing rectangular-core waveguides", Optics Letters, 13(12), 1129-1131, 1988.

[19] G. Fischbeck, R. Moosburger, M. Töpper, and K. Perterman, "Design concept for singlemode polymer waveguides", Electronics Letters, 32 (3), 212-213, 1996.

[20] R. Soref, J. Schmidtchen, and K. Petermann, "Large Single-Mode Rib Waveguides in GeSi-Si and Si-on-SiO2", IEEE Journal of Quantum Electronics, 27(8), 1971-1974, 1991.

[21] Q. Wang, S. He, and F. Chen, "An Effective and Accurate Method for the design of Directional Couplers", IEEE Journal of Selected Topics in Quantum Electronics, 8 (6), 1233-1238, 2002.

[22] M. J. Madou, Fundamentals of Microfabrication, CRC Press, Boca Raton, 1997.

[23] C. R. Pollock, Fundamentals of Optoelectronics, Irwin, Chicago, 1995.

[24] D. Marcuse, "Directional Couplers Made of Nonidentical Asymmetric Slabs. Part I: Synchronous Couplers", Journal of Lightwave Technology, 5(1), 113-118, 1987.

[25] J. P. Weber, "Spectral characteristics of coupled-waveguide Bragg-reflection tunable optical filter", Proceedings of the Institute of Electrical Engineers Part J, 140(5), 275-284, 1993.

[26] R. März, Integrated Optics: Design and Modeling, Artech House, Boston, 1995.

[27] S. S. Orlov, A. Yariv, and S. Van Essen, "Coupled-mode analysis of fiber-optic add-drop filters for dense wavelength-division multiplexing", Optics Letters, 2 (10), 688-690, 1997.

[28] N. Ofusa, T. Shimoda, T. Hanada, Y. Urino, and M. Kitamura, "An Optical Add-Drop Multiplexer with a Grating-Loaded Directional Coupler in Silica Waveguides", IEICE Transactions of Electronics, E82-C(8),1514-1517, 1999.

[29] I. Baumann and W. Nowak, "Vorteile von Optischem Frequenzmultiplex mit Faser-Bragg-Gitter-Bauelementen in Breitbandigen Passiven Faserbus-Systemen", Proceedings of MIOP '95, 638-642, 1995.

[30] K. T. Koai, and P.-L. Liu, "Modeling of Ti:LiNbO3 Waveguide Devices: Part II – S-Shaped Channel Waveguide Bends", Journal of Lightwave Technology, 7 (7), 1016-1021, 1989.

[31] R. G. DeCorby, private communication, 2002.

[32] A. Saliminia, A. Villeneuve, T. V. Galsytyan, S. LaRochelle, and K. Richardson, "First- and Second-Order Bragg Gratings in Single-Mode Planar Waveguides of Chalcogenide Glasses", Journal of Lightwave Technology, 17 (5), 837-842, 1999.

[33] H. Ma, A. K.-Y. Jen, and L. R. Dalton, "Polymer-Based Optical Waveguides: Materials, Processing, and Devices", Advanced Materials, 14(19), 1339-1365, 2002.

[34] V. K. Chagovets, E. Y. Rudavskii, D.-U. Taubenreuther, and G. Eska, "A cold valve for superfluid helium", Physica B, 284(2), 2045-2046, 2000.

[35] D. J. Beebe, D. D. Denton, R. G. Radwin, and J. G. Webster, "A silicon-based tactile sensor for finger-mounted applications", IEEE Transactions on Biomedical Engineering", 45(2), 151-159, 1998.

[36] Torlon AI-10 Bulletin: http://www.solvayadvancedpolymers.com/

[37] M. Pedersen, W. Olthuis, and P. Bergveld, "Development and fabrication of capacitive sensors in polyimide", Sensors and Materials, 10(1), 1-20, 1998.

[38] Y. Mada, S. Sugitani, K. Arai, and K. Yamasaki, "Optical properties of oxygen-ion-implanted benzocyclobutene films", Journal of Vacuum Science & Technology A, 19(3), 883-886, 2001.

[39] C. Aust, M. Kröger, and S. Hess, "Structure and dynamics of dilute polymer solutions under shear flow via nonequilibrium molecular dynamics", Macromolecules, 32(17), 5660-5672, 1999.

[40] H. Namatsu, M. Nagase, T. Yamaguchi, K. Yamazaki, and K. Kurihara, "Influence of edge roughness in resist patterns on etched patterns", Journal of Vacuum Science & Technology B, 16(6), 3315-3321, 1998.

[41] K. J. Ilcisin and R. Fedosejevs, "Direct production of gratings on plastic substrates using 248-nm KrF laser radiation", Applied Optics, 26 (2), 396-400, 1987.; D.C.D. McKen, R. Fedosejevs, M. Arnfield, I.V. Tomov, and C. Domier, "Electrically triggered multimodule KrF laser system with narrow-linewidth output", Rev. Sci. Instrum. 54 (7), 845-852, 1983.

[42] C. J. Newsome, M. O'Neill, R. J. Farley, and G. P. Bryan-Brown, "Laser etched gratings on polymer layers for alignment of liquid crystals", Applied Physics Letters, 72 (17), 2078-2080, 1998.

[43] T. Lippert, T. Gerber, A. Wokaun, D. J. Funk, H. Fukumura, and M. Goto, "Single pulse nm-size grating formation in polymers using laser ablation with an irradiation wavelength of 355 nm", Applied Physics Letters, 75 (7), 1018-1020, 1999.

[44] P. E. Dyer and J. Sidhu, "Excimer laser ablation and thermal coupling efficiency to polymer films", Journal of Applied Physics, 57 (4), 1420-1422, 1985.

[45] V.N. Tokarev, J. Lopez, S. Lazare, and F. Weisbuch, "High-aspect-ratio microdrilling of polymers with UV laser ablation: experiment with analytical model", Applied Physics A, 76, 385-396, 2003.

[46] S. Lazare and P. Benet, "Surface amorphization of Mylar fims with the excimer laser radiation above and below ablation threshold: Ellisometric measurements", Journal of Applied Physics, 74 (8), 49543-4957, 1993.

[47] J. O. Iroh, Polymer Data Handbook, Editor J. E. Mark, Oxford University Press, 1999.

[48] http://www.harrricksci.com

[49] V. Balan, C. Vigreux, A. Pradel, and M. Ribes, "Waveguides based upon chalcogenide glasses", Journal of Optoelectronics and Advanced Materials, 3 (2), 367-372, 2001.

[50] A. B. Seddon, "Chalcogenide glasses: a review of their preparation, properties and applications", Journal of Non-Crystalline Solids, 184, 44-50, 1995.

[51] G. C. Chern and I. Lauks, "Spin-coated amorphous chalcogenide films", Journal of Applied Physics, 53 (10), 6979-6982, 1982.

[52] G. C. Chern and I. Lauks, "Spin coated amorphous chalcogenide films: Structural characterization", Journal of Applied Physics, 54 (5), 2701-2705, 1983.

[53] O. Nordman, N. Nordman, and V. Pashkevich, "Influence of ultraviolet-light exposure on electron-beam written gratings in amorphous As-Se thin films coated with different metals", Applied Physics Letters, 79 (13), 2004-2006, 2001.

[54] N. I. Anisimova, G. A. Bordovsky, V. A. Bordovsky, and R. A. Castro, "The photoinduced change of dissolution rate in As_2Se_3 glasses", Radiation Effects and Defects in Solids, 156(1-4), 365-369, 2001.

[55] V. Lyubin, M. Klebanov, I. Bar, S. Rosenwaks, N. P. Eisenberg, and M. Manevich, "Novel effects in inorganic $As_{50}Se_{50}$ photoresists and their application in micro-optics", Journal of Vacuum Science & Technology B, 15 (4), 823-827, 1997.

[56] A. L. Dawar, P. K. Shishodia, G. Chauhan, J. C. Joshi, C. Jagadish, and P. C. Mathur, "Effect of UV exposure on optical properties of amorphous As_2S_3 thin films", Applied Optics, 29 (13), 1971-1973, 1990.

[57], T. Augustsson, "Bragg Grating-Assisted MMI-Coupler for Add–Drop Multiplexing", Journal of Lightwave Technology, 16(8), 1517-1522, 1998.

[58] S. H. Messaddeq, M. S. Li, D. Lezal, S. J. L. Riberiro, and Y. Messaddeq, "Above bandgap induced photoexpansion and photobleaching in Ga-Ge-S bases glasses, Journal of Non-Crystalline Solids, 284(1-3), 282-287, 2001.

[59] S. H. Messaddeq, M. S. Li, D. Lezal, and Y. Messaddeq, "Relief grating induced by photo-expansion in Ga-Ge-S and Ga-Ge-As-S glasses", Journal of Optoelectronics and Advanced Materials", 4(2), 374-380, 2002.

[60] C. R. Schardt, J. H. Simmons, P. Łucas, L. Le Neindre, and J. Lucas, "Photodarkening in Ge3Se17 glass", Journal of Non-Crystalline Solids, 274(1-3), 23-29, 2000.

Appendix 1: Oversized Rib Waveguide Criteria

Rib waveguides form the waveguide structure in the majority of passive integrated optical devices [1]. Criteria for singlemode rib waveguides with large cross sections has been developed from the effective index method and numerical analysis [2], [3], [2], facilitating fabrication and connection of components due to an increase in waveguide dimensions.

The single mode criteria results in scaling rules on the rib width (w), side slab height (h), and rib height (H) for which single mode operation exists (Fig. A1.). As the rib structure is increase in size the scaling relations ensure that the higher order modes couple to modes in the side slabs; resulting in these modes being radiated during propagation [3] and singlemode operation.

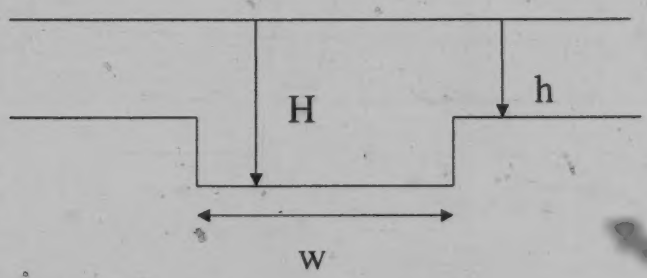

Figure A1.1: Cross Section of Inverted Rib Waveguide. Scaling the rib width (w), side slab height (h), and rib height (H) according to the oversized rib criteria allows single mode operation for large cross sections.

The calculation of large singlemode structures requires basic, but tedious, numerical solution. With the intent of allowing back of the envelope calculation of large singlemode structures, simplified scaling relations are sought.

The singlemode propagation criteria was developed by Soref *et al.* [3] from Petermann [2] and further investigated by Pogossian *et al.* [1]. The conditions are

$$0.5 \le r < 1, \tag{A1.1}$$

and

$$t < c + \frac{r}{\sqrt{1-r^2}}, \tag{A1.2}$$

where $t=w_{eff}/H_{eff}$, $r=h_{eff}/H_{eff}$, $h_{eff}=h+q$, $H_{eff}=H+q$, $w_{eff}=w+p$, $q=\gamma_c/\{k(n_f^2-n_c^2)^{1/2}\}+\gamma_s/\{k\Delta\}$, $p=2\gamma_c/\{k(n_f^2-n_c^2)^{1/2}\}$, $n_f>n_s>n_c$ are the refractive indices of the guiding film, substrate, and cladding respectively, $\Delta=(n_f^2-n_s^2)^{1/2}$, $\gamma_{c,s}$ is 1 for TE modes and $(n_{c,s}/n_f)^2$ for TM modes, $k=2\pi/\lambda$, and λ is the wavelength. The c parameter is used to empirically fit to experiment, and is given as –0.05 by Pogossian *et al.*

We seek to draw out the salient features of the scaling rules, and mold them in terms of physical parameters. Examining equation (A1.1) we see

$$1 > \frac{h+q}{H+q} \ge 0.5.$$

Noting that $(h+q)/(H+q) > (h/H)$, as $H>h$ and $q>0$, we can make the following conservative approximation

$$H > h \ge \frac{H}{2}. \tag{A1.3}$$

Turning to equation (A1.2) we first set the empirical fitting constant to zero, resulting in an easier to handle inequality[1]. Simple manipulations show that $p<q$ for both TE and TM modes, and thus we have

[1] The fitting parameter is a "hidden variable", which allows the effect of unaccounted for variables to be incorporated. Fitting parameters can be applied to any equation, and essentially act as a flag signaling the exclusion of significant variables. Excluding this parameter does not affect the underlying model, and can

$$\frac{(w+q)}{(H+q)} < \frac{(h+q)/(H+q)}{\sqrt{1-\left(\frac{h+q}{H+q}\right)^2}}.$$

The square root term is roughly equal to one, and we drop it to simplify things to

$$w < h. \qquad \text{(A1.4)}$$

The simplified scaling relations defined by (A1.3) and (A1.4) display a linear boundary and require a single computation, which is simply half the ribs thickness. In addition the relations are valid for both TE and TM polarization, forming unified criteria for singlemode operation. The removal of the core and cladding index from the equations was dependent on assuming that q>0 (i.e. a guiding system exists), and indicts that the geometry of an oversized rib waveguide largely determines the behavior.

Care must be taken, as the lack of dependence on the index of refraction suggests that these scaling rules are overly simplified. Taking a closer look with numerical investigations shows that, for many material systems, there is surprising agreement between the different scaling rules, when fabrication error is taken into account (typically 0.5 microns for single pass design cycles). Table A1.1 tabulates the h_{min} and w_{max} values for air clad deep ribs (where the minimal allowed side slab is used) with TE polarized 1.55 μm light. As the p and q values in the full scaling rules are smaller for TM modes the TE solution presents the worse case scenario. The Δ range spans readily available values, with the low bound set by flame hydrolysis deposition of glass on silica and the upper bound by silicon on insulator (SOI).

---

be reincorporated back into modified equations at will. In any case we seek guiding principles, which are conservative, eliminating the need for such parameters.

Table A1.1 Comparison of scaling rule sets. Here air clad 8 μm film with TE polarized 1.55 μm light is assumed.

Materials	Δ	h_{min} from (1)	h_{min} from (3)	w_{max} from (2)	w_{max} from (4)
Silica Flame Hydrolysis	0.0045 [4]	-2.3526	4	3.2972	4
Silicon Oxynitride	0.2378 [5]	3.3687	4	4.6088	4
GaAs-AlGaAs	0.5061 [6]	3.7193	4	4.3786	4
GaInAsP-InP	1.2293 [7]	3.8617	4	4.2254	4
Chalcogenide	1.7772 [8]	3.8710	4	4.1581	4
Silicon on Insulator	3.1855 [3]	3.9245	4	4.1629	4

At low confinement the simplified rules show substantial (~ μm) divergence from the full rules. As confinement is increased the predicted values rapidly approach those given by the full rules. Table A1.2 lists the minimum Δ value required for the different scaling rule sets to agree within given measures, for air clad deep ribs excited with 1.55 μm TE polarized light. Strictly speaking Δ alone cannot be used as a parameter, due to the $(n_f^2-n_c^2)^{1/2}$ term in q forcing the presence of n_f to be felt. Practically speaking, n_f values lie between 1.4 (specialized polymers) and 3.6 (low band gap semiconductors), if we force n_f to take its maximal value larger Δ values are calculated. This highly artificial situation allows Δ to be used as a convenient and strict measure, guaranteeing the desired accuracy is met or surpassed. It is interesting that the full scaling rules give a negative dimension for the minimum side slab height at ultra-low confinement – this is an artifact of the

"effective" dimensions used, demonstrating that for ultra-low confinement the scaling rules break down (errors in approximations often run away near cut-off)[2].

Table A1.2 Minimum Δ required for simplified rules. Here the minimum Δ for the simplified rules to be valid within a given measure is found, for deep rib guides excited with 1.55 μm TE polarized light.

Rib height H (μm)	Δ_{min} for 1 μm agreement	Δ_{min} for 0.5 μm agreement	Δ_{min} for 0.25 μm agreement
2	0.1251	0.2410	0.4490
4	0.1321	0.2682	0.5535
6	0.1398	0.3023	0.7214
8	0.1486	0.3463	1.0355
10	0.1585	0.4054	1.8341

To give an impression of just how conservative the Δ values given in Table A1.2 are, if n_f is set to 2.0 the minimum Δ for the different rules to agree within 0.25 μm for a 10 μm high rib is 1.0660 (and is 0.3817 for a 2 μm tall rib). It should be noted that an older, but still common, variant of the full scaling relations where c=0.3 [3] gives structure dimensions that deviate much more than the simplified equations (~ 1 μm or more for most structures, versus the ~ 1 μm maximum for the simplified rules). As shown by Pogossian *et al.* [1] this variant over predicts allowable structure size, resulting in some structures being multimoded, while the full scaling rules lies on the boundary between single and multimode operation.

The consistency between the rule sets rolls off as we move away from the deep rib criteria, by increasing h. As an example, if we set h to 6 μm for a 8 μm tall SOI rib the full rules dictate that w must be less than 8.8 microns. This result is substantially different than the 6 μm bound set by the simplified rules, and should be kept in mind when

---

[2] Note that $q \sim \frac{\lambda}{\Delta}$ with λ≈h,H and Δ≅[0,4]. q can therefore become quite large for low confinement. Looking at A1.1 we see that negative values for h are not surprising.

designing shallow ribs. In practice deep ribs are generally preferred, as they reduce the asymmetry of the waveguide mode mapping into lower in-coupling losses and better predictability as well as better lateral confinement. A survey of literature citing [1] and [3] bares this out, with implementations of rib guides tending towards deep ribs.

The simplified rules proposed here are conservative, polarization independent, and exceedingly simple in form. Due to a lack of dependence on the index of refraction the rules become increasingly conservative for low Δ waveguides, forming the major weakness of the simplified rules. For many material systems the simplified rules give results close in value to the full rules, if $\Delta > 0.4$ the simplified rules are guaranteed to be accurate within 0.5 microns and in practice oversized cross section rib waveguides are required only for large Δ systems. Given that the simplified rules offer clarity, are more accurate then a common full rule variant, and give conservative estimates close in value to the full rules, the simplified scaling rules form excellent design equations for large cross section rib waveguides.

References

[1] S. P. Pogossian, L. Vescan, and A. Vonsovici, "The single-mode condition for semiconductor rib waveguides with large cross section", Journal of Lightwave Technology, 16(10) 1851-1853, 1998.

[2] K. Petermann, "Properties of optical ribguides with large cross-section", AEU International Journal of Electronics and Communications, 30(3), 139-140, 1976.

[3] R. Soref, J. Schmidtchen, and K. Petermann, "Large Single-Mode Rib Waveguides in GeSi-Si and Si-on-SiO2", IEEE Journal of Quantum Electronics, 27(8), 1971-1974, 1991.

[4] J. M. Ruano, V. Benoit, J. S. Aitchison, and J. M. Cooper, "Flame hydrolysis deposition of glass on silicon for the integration of optical and microfluidic devices", Analytical Chemistry, 72(5), 1093-1097, 2000.

[5] K. Wörhoff, P. V. Lambek, and A. Driessen, "Design, tolerance analysis, and fabrication of silicon oxynitride based planar optical waveguides for communication devices", Journal of Lightwave Technology, 17(8), 1401-1407, 1999.

[6] J. M. Heaton, M. M. Bourke, S. B. Jones, B. H. Smith, K. P. Hilton, G. W. Smith, C. H. Birbeck, G. Berry, S. V. Dewar, and D. R. Wight, "Optimization of deep-etched, single-mode GaAs/AlGaAs optical waveguides using controlled leakage into the substrate, Journal of Lightwave Technology, 17(2), 267-281, 1999.

[7] R. Grover, P. P. Absil, V. Van, J. V. Hryniewicz, B. E. Little, O. King, L. C. Calhoun, F. G. Johnson, and P. T. Ho, "Vertically coupled GaInAsP-InP microring resonators", Optics Letters, 26(8), 506-508, 2001.

[8] S. Spälter, H. Y. Hwang, J. Zimmermann, G. Lenz, T. Katsufuji, S. W. Cheong, and R. E. Slusher, "Strong self-phase modulation in planar chalcogenide glass waveguides", Optics Letters, 27(5), 363-365, 2002.

Appendix 2: Swanepoel's Method

The availability of spectrophotometers allows optical response (typically transmission spectra) to be measured. As the index of refraction acts as the fingerprint of a materials interaction with light we wish to find this index. Given an index profile the transfer matrix method can find the response of an optical system. Unfortunatly the inverse problem of finding an index profile from a desired response is difficult, limiting the effectiveness of the transfer matrix method for finding refractive indices or structures that give a desired response.

The transmissin response for a thin film is shown in Fig. A2.1. Wavelengths where minima and maxima occur in the transmission profile are called interference wavelengths.

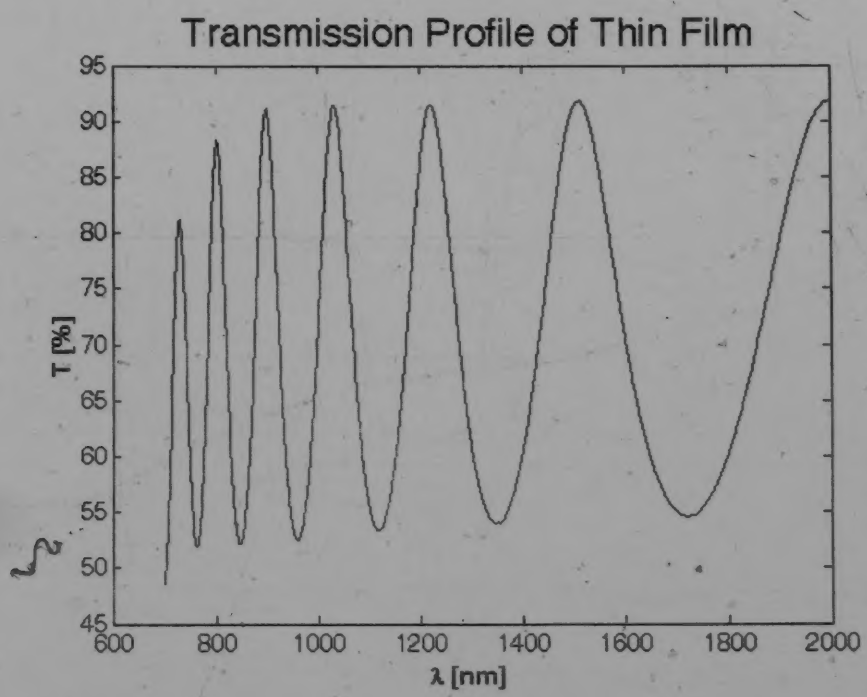

Figure A2.1 Transmission response of a thin film. The measured transmission for a ~1.1 μm thick chalcogenide film demonstrates the interference pattern typical of thin films.

Swanepoel's method allows the refractive index and a film's thickness to be determined using transmission values at interference wavelengths. As interference occurs for specific n, d, λ values taking a set of transmission values, at known interference wavelengths, gives insight into the value of the index (multiplied by the film thickness) at these wavelengths. By using the envelope of transmission minima and maxima at the interference wavelengths the index can be extract, if the film is weakly absorbing [1]. Swanepoel extended the work of Manifacier *et al.* [1] allowing the refractive index and film thickness to be calculated for both weakly and mildly absorbing films [2]. The method is applicable to uniform thin films, and has been used successfully on thin chalcogenide films fabricated with thermal evaporation [3].

For transparent wavelengths the transmission values at the interference minima fringes allow the index can be found from [1], [2]

$$n = \left(M + \sqrt{M^2 - s^2}\right)^{\frac{1}{2}}$$
$$M = \frac{2s}{T_m} - \frac{s^2 + 1}{2} \qquad \text{(A2.1)}$$

where T_m is the transmission value at minima fringes, and s is the index of the substrate the film is deposited on. Improvements in the above formula set are obtained by modifying M according to more detailed analysis [2]. When the film weakly absorbs M is modified to [2]

$$M = 2s\frac{T_M - T_m}{T_M T_m} + \frac{s^2 + 1}{2}, \qquad \text{(A2.2)}$$

and loss can be found from the following equation set,

$$x = e^{-\alpha d}$$

$$x = \frac{E_M - \left[E_M^2 - (n^2-1)^3(n^2-s^4)\right]^{\frac{1}{2}}}{(n-1)^3(n-s^2)}, \qquad \text{(A2.3)}$$

$$E_M = \frac{8n^2 s}{T_M} + (n^2-1)(n^2-s^2)$$

where T_M is the transmission at maxima fringes. The losses can only be accurately determined in the strongly absorbing region ($\alpha > 10^4$ dB/cm) [3]; accuracy rapidly drops off as α decreases in value. This limits the use of loss estimates to finding the optical band gap; finding loss in near transparent regions must rely on other methods.

The index of the substrate can be found from [3]

$$s = \frac{1}{T_s} + \left(\frac{1}{T_s} - 1\right)^{\frac{1}{2}}. \qquad \text{(A2.4)}$$

For this approach to be applicable the index should be uniform through the film and the film should have a constant thickness. When these conditions are met the relative error in the refractive index found is approximately an order of magnitude larger than error in the transmission values [2], which for commercial spectrometers sets index error to ~ 1%. This low error combined with the simple, nondestructive, measurement process makes Swanepoel's method highly useful.

References

[1] J. C. Manifacier, J. Gasiot, and J. P. Fillard, "A simple method for the determination of the optical constands n, k and the thickness of a weakly absorbing thing film", Journal of Physics E, 9(11), 1002-1004,1976.

[2 R. Swanepoel, "Determination of the thickness and optical constants of amorphous silicon", Journal of Physics E, 16 (12), 1214-1222, 1983.

[3] E. Márquez, J. Ramírez-Malo, P. Villares, R. Jiménez-Garay, P. J. S. Ewan, and A. E. Owen, "Calculation of the thickness and optical constants of amorphous arsenic sulphide films from their transmission spectra", Journal of Physics D, 25(3), 535-541, 1992.